# HIGH-RESOLUTION DYNAMIC MAPPING OF HISTONE-DNA INTERACTIONS IN A NUCLEOSOME THROUGH THE USE AND DEVELOPMENT OF NOVEL OPTICAL TRAPPING TECHNIQUES

A Dissertation

Presented to the Faculty of the Graduate School

of Cornell University

In Partial Fulfillment of the Requirements for the Degree of

Doctor of Philosophy

by

Michael Anthony Hall

January 2011

© 2011 Michael Anthony Hall

# HIGH-RESOLUTION DYNAMIC MAPPING OF HISTONE-DNA INTERACTIONS IN A NUCLEOSOME, THROUGH THE USE AND DEVELOPMENT OF NOVEL OPTICAL TRAPPING TECHNIQUES

Michael Anthony Hall, Ph.D.

Cornell University 2011

The nucleosomal barrier regulates access to the underlying DNA during many cellular processes. In Chapter 3, we present a detailed map of histone-DNA interactions along the DNA sequence to near base pair accuracy by mechanically unzipping single molecules of DNA, each containing a single nucleosome. This interaction map revealed a distinct 5-bp periodicity that was enveloped by three broad regions of strong interactions, with the strongest occurring at the dyad and the other two about ±40-bp from the dyad. Unzipping up to the dyad allowed recovery of a canonical nucleosome upon relaxation of the DNA, but unzipping beyond the dyad resulted in removal of the histone octamer from its initial DNA sequence. These findings have important implications for how RNA polymerase and other DNA-based enzymes may gain access to DNA associated with a nucleosome. Two novel optical trapping techniques are described in Chapters 4 and 5, respectively: the adaptation of the unzipping method to apply to new biological assays and a novel microfluidic flow cell compatible with single molecule optical trapping experiments. These developments expand the role that optical trapping plays in the study of biological questions.

## BIOGRAPHICAL SKETCH

Michael Anthony Hall was born in Langhorne, PA on the summer solstice of 1980. He attended Conwell-Egan Catholic High School in Fairless Hills, PA. In 1998 he attended Drexel University in Philadelphia, PA and earned a Bachelors of Science in Physics in 2003. Upon acceptance to the graduate program at Cornell University, he moved to Ithaca, NY. He joined the lab of Michelle D. Wang in 2005, graduated with a Masters of Science in 2008 and a Ph.D. in 2010.

*To my family, especially my mother, Kathie, my grandmother, Carrie, and my grandfather, Roy. Their unwavering support has been truly inspirational.*

# ACKNOWLEDGMENTS

First, I need to thank my advisor, Michelle D. Wang, for her invaluable scientific advice. The training that I have received in this laboratory has been wide and far-reaching, a unique accumulation of skills that I would be hard pressed to have found anywhere else. Secondly, I have very much appreciated the opportunity to have studied alongside an amazing group of students. Each of them has brought unique talents to the group and I have benefited via countless discussions and exchange of ideas with them. In addition, I want to thank the following coworkers for providing, in various ways, a tremendous amount of emotional support, above and beyond what is normally expected, during the long, often arduous journey: Scott Forth, Jing Jin, Daniel Johnson, Ming Li, Thibault Roland, Maxim Sheinin, and Benjamin Smith. I would also like to thank my special committee members, John Lis, Veit Elser and W. Lee Kraus for both scientific feedback and encouragement over the years.

I offer my sincerest thanks to my family who have supported and encouraged me throughout my entire life to pursue those interests I hold dear, both within the scientific field and without. My mother, Kathie, deserves the most recognition for, at times, almost daily support during periods of greatest frustration. My grandparents, Carrie and Roy, have consistently encouraged me to do my best and, in fact, it was largely the result of reflections on conversations I've had with my grandfather, Roy Finley, that inspired me to reach my full potential. Most recently, I really appreciate the support of my sister, Michele Hall, my step father, Jack Costello, and my aunts, uncles and cousins who provided so much encouragement during the final few months: Krista Hall and Rick Doran, Laura Hall, Karen Hall, Pattie Medvic and Jamie and Christine O'Brien.

Finally, I also thank my friends who have consistently supported me throughout my academic pursuits by making every day a pleasure. They've also offered mental and emotional support, often by listening to me vent about experiments and the life of being a graduate student. There are too many people to list here, but I want to especially recognize Samantha Allen, Patrick Bradley, Li-Wei Chiu, Remus Dame, Fumiko Kawazoe, Jing Jin, Ming Li, Judson Powers, Janet Shen, Isabelle Smith, and Megan Thompson. Most of all, I thank Yue Shi, whose special friendship has provided me with so much joy that it removes all doubt whether or not the struggles of graduate life over the past 7 years have been truly worth it.

TABLE OF CONTENTS

LIST OF FIGURES

# Chapter 1:
# The Nucleosome

***The nucleosome as a barrier to translocation enzymes***

Eukaryotic cells, considering their microscopic size, are impressively versatile. Even single cells are capable of exerting forces (e.g. cellular movement, muscle contraction, separation of chromosomes), transporting molecules against chemical gradients, generating heat and electric potentials, transforming their own environment (e.g. extra-cellular matrix), self-replication and communication with neighboring cells, all powered through photosynthesis or respiration. Equally impressive is that all of these functions are coupled to a feedback mechanism whereby cells actively respond to external stimuli from their environment. Each action requires the involvement of large numbers of molecular motors, perfectly constructed, working in concert with one another. The blueprints for these molecular motors, the genetic code, are haphazardly stored along the DNA. But what ultimately orchestrates the fabrication of individual cellular components is a poorly understood assortment of DNA-binding proteins and methylated DNA bases meticulously arranged in a coordinated manner that regulate access to the genetic code by providing signals that determine its local structure and, therefore, its accessibility and potential for information retrieval[1,2,3,4]. In this way, the existing cellular machinery is directed as to how it should organize and efficiently utilize its existing means of production. This code, like an adaptable software algorithm, continuously changes in response to existing inner and extra-cellular conditions to ensure the long term survival of the cell. Thus, the central processing unit of the eukaryotic cell exists within the nucleus and chromatin is at its core. Its accessibility is determined by both its local geometry and its large-scale compaction mechanism. In all likelihood, the cell has evolved a technique to accommodate the greatest level of compaction without adversely affecting the biological processing described above.

Relative to the diameter of a typical cell (~ 10 μm), the genetic code is enormous: a molecule stretching nearly two meters in length! As a result, solving the compaction problem is non-trivial. After decades of research, we are surprisingly ignorant of exactly how the cell accomplishes this monumental task. At the highest level, chromatin can be observed via light microscopy in the form of the familiar 'X'-shaped chromosomes ~ 750 nm thick when its condensation is maximized during cell division. Their overall shape appears to be maintained through a network of proteins[5] that form a scaffold along the axes of the two chromosomal arms[6]. Microscopic analyses performed during prophase have provided inconclusive evidence for at least two levels of compaction below fully compacted chromatids, but modeling has proven to be difficult[7].

At the lowest level, crystallography has revealed that DNA wraps nearly twice around an octamer of histone proteins forming a structure known as the nucleosome[8,9] (Figure 1a) approximately every 200 base pairs (bp) throughout the genome. The histones interact strongly with the DNA at each minor groove, simultaneously neutralizing some of the negative charge on the DNA[10]. Charge neutralization decreases its persistence length[11] allowing it to bend around the histone core more tightly than it could otherwise. The nucleosome often constitutes a major barrier for motor proteins that translocate along DNA[12,13] although this is partially alleviated because the DNA at the entry/exit points of the nucleosome fluctuates rapidly, effectively permitting its own invasion[14,15,16]. The addition of linker histones prevents this, when necessary, by simultaneously binding in the vicinity of the nucleosomal dyad and to one or both of the entry/exit DNA strands. In the presence of linker histone, long arrays of nucleosomes cooperatively fold into a fiber ~ 30 nm thick, although the geometry of this fiber has been hotly debated for decades[17,18]. Even the model of linker histone

**Figure 1.1 Crystal structure of the nucleosome adapted from Luger et al. (1997).** The core of the nucleosome consists of two copies each of two histone protein dimers: H2A/H2B (yellow / red) and H3/H4 (blue / green). The two H3/H4 dimers form a tetramer via a bundle of 4 alpha helices at the symmetry point of the nucleosome (known as the dyad). Each H2A/H2B dimer docks primarily onto the H3/H4 tetramer and have minimal contact with each other. Positively charged residues form a helical ramp around the outer edge of the histone core which neutralizes the negative charge on the DNA backbone and wraps 147 bp around its surface in 1.6 negative superhelical turns.

binding is under debate and several different models have been proposed[19,20,21].

In addition to chromatin compaction, the nucleosome plays a critical role in the regulation of genetic expression. What makes, say, a red blood cell different than a neuron are differences in the genetic expression levels of the identical gene set contained within each cell. Nucleosomes arguably play the most important role through their careful placement throughout the genome, selectively occluding access to a particular set of "start sequences" called promoters and/or providing sequential barriers to the elongation of RNA polymerases[12,13,22,23,24,25] (Figure 1.2a). For genes that must be actively transcribed, the nucleosomal barrier must be efficiently removed. In other cases, the nucleosomal barrier is beneficial by preventing premature or errant RNA polymerase activity. In any event, a thorough understanding of the nature of the nucleosomal barrier is critical to the understanding of how translocation (RNA polymerases, helicases, etc.) (Figures. 1.2a-b) or remodeling enzymes (SWI/SNF, ACF, Chd1, etc.) (Figure 1.2c) overcome it.

Many experiments rely upon some form of imaging – for example, crystallography or electron microscopy. These techniques obviously lend themselves well to structural studies, but they also have very critical limitations. Crystallography has revealed the atomic structure of the nucleosome in unprecedented detail[9] (1.9 Å). For the study of relatively simple structures, it can't be beat in terms of spatial resolution. However, it is severely limited in its ability to estimate precise interaction locations and strengths. Estimates from crystal structures typically involve counting the number of perceived interactions[8,26]. In contrast, the strength of our lab is rooted in our ability to quantify the forces and displacements involved in biological processes. The mechanical nature of the nucleosomal barrier makes optical trapping techniques well-suited for the

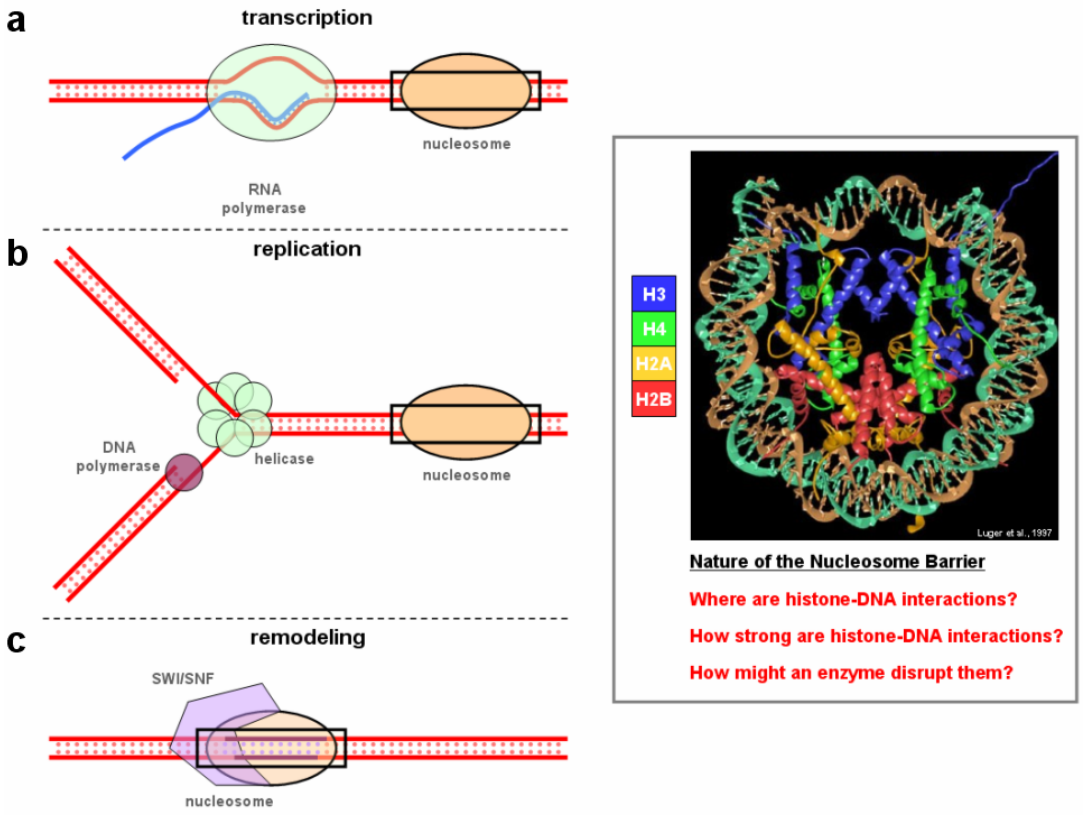


**Figure 1.2 Histone-DNA interactions in a nucleosome as a barrier.** Translocation enzymes such as (a) RNA polymerases and (b) DNA helicases regularly deal with the nucleosome as a barrier to translocation. Whether these enzymes overcome the barrier through direct contact or via the coordination of histone chaperones is still an area of active research. Knowledge of the histone-DNA interaction map reveals the most probable stalling locations and which interactions are most vital to disrupt in order to achieve complete nucleosome traversal. (c) The action of nucleosome remodeling enzymes, also a widely debated topic in the literature, may largely be dictated by their involvement in efficient histone removal and/or repositioning; for example, the disruption of only the strongest interactions.

treatment of this problem.

***Previous work – stretching nucleosomal arrays***

In the stretching configuration, a dsDNA molecule containing well-positioned nucleosomes is chemically attached at one end to the surface of a microscope coverslip while the other end is chemically attached to a polystyrene bead[27]. The molecule is stretched by holding the bead in an optical trap[28] and moving the cover slip away from the trap via a piezoelectric stage (Figure 1.3a). The downstream power and deflection of the laser beam is monitored, providing real time information about the disruption of the nucleosome via the force and extension along the length of the molecule. Since force-extension pairs uniquely determine the contour length of the molecule[29], the number of base pairs can be calculated at all times. Figure 1.3b shows data taken on an array of 17 nucleosomes that have been assembled on a DNA sequence composed of 17 semi-periodic naturally occurring nucleosome positioning elements (NPE). As the molecule was extended, the force deviated significantly from that expected for naked DNA (Figure 1.3b, red dotted line). Above an extension of 700 nm, 17 distinct peaks in the force were observed, presumably a reflection of a saturated array of assembled nucleosomes. In each case, the disruption is correlated with a release of ~ 75 bp of DNA[27]. Below 700 nm extension, the discrepancy in the force between the assembled array and that expected for naked DNA is correlated with a slow, continuous increase in the number of base pairs along the length of the molecule[27]. These observations have been interpreted as DNA being slowly peeled from either side of the "outer turn" of the nucleosome at low force and a sudden disruption of the "inner turn" at high force. This interpretation implies the existence of uniformly weak histone-DNA interactions up to ~ 35 bp from either edge of the

nucleosome and a region of slightly stronger histone-DNA interactions ~ 35-40 bp on either side of the dyad, as indicated in Figure 1.3c.

While this interpretation of the data is feasible, publication of this work led to an open discussion in the literature as to whether or not the dominant energy barrier involved in nucleosome disruption under dsDNA tension could actually be attributed to non-uniform DNA-histone affinity[30,31,32]. Studies from both an experimental and theoretical framework challenged our interpretation, suggesting that the rotation of the nucleosome about its axis during the disruption event could explain our nucleosome stretching experiments while maintaining the assumption of uniform histone-DNA interaction profile.

The controversy is partially the result of some limitations of using the stretching configuration for the study of nucleosome structure. First, the stretching method cannot separate the relative energy contributions from (a) histone-DNA affinity and (b) the rotation of the nucleosome about its axis. Secondly, the stretching method can only detect *relative* changes in the extension. For example, whereas our interpretation of the stretching data is that the DNA peeled off the outer turn of the nucleosome comes from each side of the nucleosome equally, another possible interpretation is that one side peels off more readily than the other. Finally, the stretching configuration cannot physically probe histone-DNA interactions at the nucleosomal dyad, what are commonly believed to be the most important interactions of all.

As discussed in Chapter 3, to conclusively settle the controversy discussed above and to deliver a high-resolution map of histone-DNA affinity, we used an optical trap to separate the two strands of DNA at a constant force. Histone-DNA affinity was

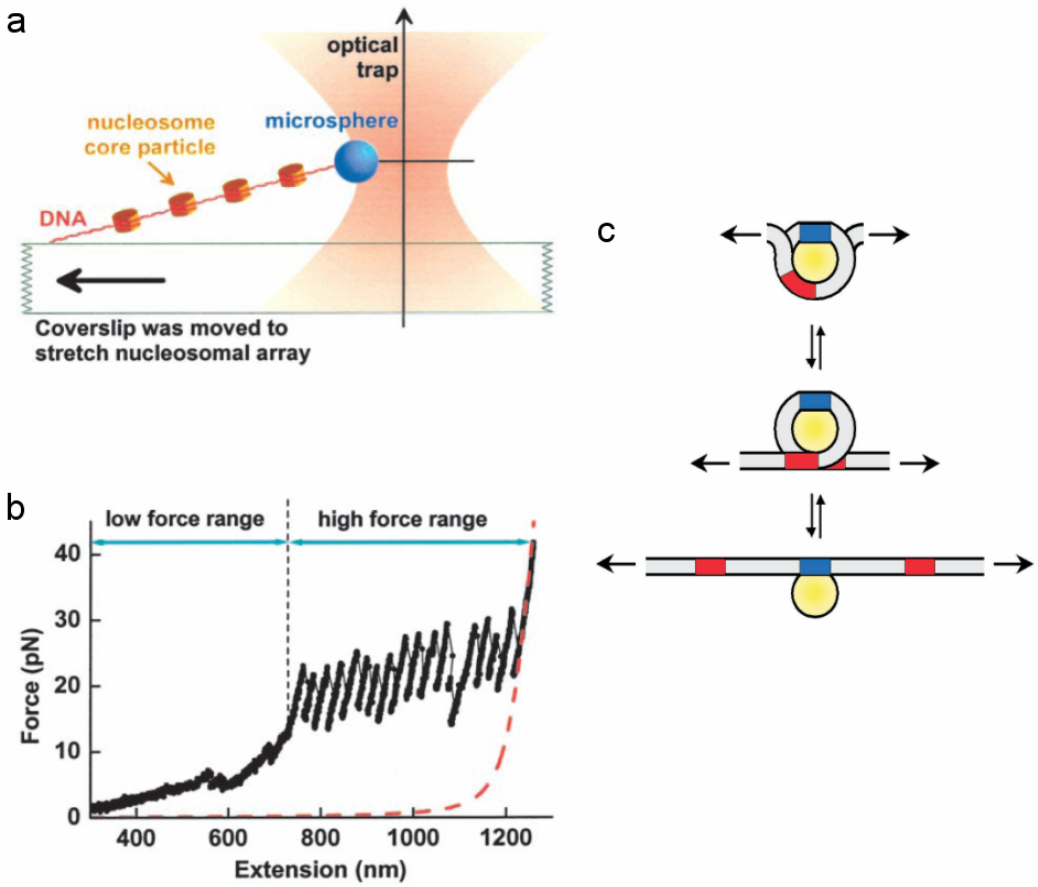


**Figure 1.3 Nucleosome stretching experiments, adapted from Brower-Toland et al. (2002).** (a) Experimental configuration for stretching dsDNA with assembled nucleosomes in an optical trap. (b) Representative force-extension data for a saturated array of 17 well-positioned nucleosomes. The force-extension expected for naked dsDNA is indicated by the red dotted line. See text for details. (c) The stepwise model of nucleosome dissociation under applied force. The first stage occurs via slow, continuous peeling. The existence of strong regions of interaction (red), symmetric about the dyad, causes the next stage to occur rapidly. With the disruption of the strong regions of interaction, weaker internal interactions are immediately disrupted with it. Very strong interactions in the vicinity of the dyad (blue) are postulated because reversibility studies demonstrated that the histone octamer often remains on the dsDNA even after its disruption signature has been observed (data not shown).

determined by measuring the dwell time of the unzipping fork at each base pair. These data ultimately confirm our original interpretation of the stretching data and reveal significant new information about the structure of histone-DNA interactions in a nucleosome and nucleosome stability.

REFERENCES


1. Strahl, BD and Allid CD, The language of covalent histone modifications. *Nature* **403**(6765): 41-5 (2000).
2. Jenuwein, T. and Allis CD, Translating the histone code. *Science* **293**(5532): 1074-80 (2001).
3. de la Cruz, X., Lois S, Sanchez-Molina S and Martinez-Balbas MA. Do protein motifs read the histone code? Bioessays **27**(2): 164-75 (2005).
4. Kouzarides, T, Chromatin modifications and their function. *Cell* **128**(4): 693-705 (2007).
5. Poirier, MG and Marko JF, Mitotic chromosomes are chromatin networks without a mechanically contiguous protein scaffold. *Proc Natl Acad Sci U S A* **99**(24): 15393-7 (2002).
6. Maeshima, K and Eltsov M, Packaging the genome: the structure of mitotic chromosomes. *J Biochem* **143**(2): 145-53 (2008).
7. Kireeva, N., M. Lakonishok, I. Kireev, T. Hirano and A. S. Belmont, Visualization of early chromosome condensation: a hierarchical folding, axial glue model of chromosome structure. *J Cell Biol* **166**(6): 775-85 (2004).
8. Luger, K, Mader AW, Richmond RK, Sargent DF and Richmond TJ, Crystal structure of the nucleosome core particle at 2.8 A resolution. *Nature* **389**(6648): 251-60 (1997).
9. Davey, CA, Sargent, DF, Luger, K., Maeder, AW and Richmond, TJ, Solvent mediated interactions in the structure of the nucleosome core particle at 1.9 Å resolution. *J Mol Biol* **319**, 1097-113 (2002).
10. Manning, GS, Is a small number of charge neutralizations sufficient to bend nucleosome core DNA onto its superhelical ramp? *J Am Chem Soc* **125**(49): 15087-92 (2003).

11. Podesta, A, Indrieri M, Brogioli D, Manning GS, Milani P, Guerra R, Finzi L and Dunlap D, Positively charged surfaces increase the flexibility of DNA. *Biophys J* **89**(4): 2558-63 (2005).

12. Kireeva, ML, Hancock B, Cremona GH, Walter W, Studitsky VM and Kashlev M, Nature of the nucleosomal barrier to RNA polymerase II. *Mol Cell* **18**(1): 97-108 (2005).

13. Bondarenko, VA, Steele LM, Ujvari A, Gaykalova DA, Kulaeva OI, Polikanov YS, Luse DS and Studitsky VM, Nucleosomes can form a polar barrier to transcript elongation by RNA polymerase II. *Mol Cell* **24**(3): 469-79 (2006).

14. Li, G. and Widom J, Nucleosomes facilitate their own invasion. *Nat Struct Mol Biol* **11**(8): 763-9 (2004).

15. Li, G, Levitus M, Bustamante C and Widom J, Rapid spontaneous accessibility of nucleosomal DNA. *Nat Struct Mol Biol* **12**(1): 46-53 (2005).

16. Tomschik, M., Zheng H, van Holde K, Zlatanova J and Leuba SH, Fast, long-range, reversible conformational fluctuations in nucleosomes revealed by single-pair fluorescence resonance energy transfer. *Proc Natl Acad Sci U S A* **102**(9): 3278-83 (2005).

17. Tremethick, DJ, Higher-order structures of chromatin: the elusive 30 nm fiber. *Cell* **128**(4): 651-4 (2005).

18. van Holde, K. and Zlatanova J, Chromatin fiber structure: Where is the problem now? *Semin Cell Dev Biol* **18**(5): 651-8 (2005).

19. Bharath, MM, Chandra NR and Rao MR, Molecular modeling of the chromatosome particle. *Nucleic Acids Res* **31**(14): 4264-74 (2003).

20. Brown, DT, Izard T and Misteli T, Mapping the interaction surface of linker histone H1(0) with the nucleosome of native chromatin in vivo. *Nat Struct Mol Biol* **13**(3): 250-5 (2006).

21. Fan, L and Roberts VA, Complex of linker histone H5 with the nucleosome and its implications for chromatin packing. *Proc Natl Acad Sci U S A* **103**(22): 8384-9 (2006).

22. Kireeva ML, Walter W, Tchernajenko V, Bondarenko V, Kashlev M, and Studitsky VM, Nucleosome remodeling induced by RNA polymerase II: loss of the H2A/H2B dimer during transcription. *Mol. Cell* **9**(3): 541-552 (2002).

23. Studitsky, VM, Kassavetis, GA, Geiduschek, EP and Felsenfeld, G, Mechanism of transcription through the nucleosome by eukaryotic RNA polymerase. *Science* **278**, 1960-3 (1997).

24. Studitsky, V.M., Walter, W., Kireeva, M., Kashlev, M. & Felsenfeld, G. Chromatin remodeling by RNA polymerases. *Trends Biochem Sci* **29**, 127-35 (2004).

25. Walter, W., Kireeva, M.L., Studitsky, V.M. & Kashlev, M. Bacterial polymerase and yeast polymerase II use similar mechanisms for transcription through nucleosomes. *J Biol Chem* **278**, 36148-56 (2003).

26. Luger, K. and Richmond, T.J. DNA binding within the nucleosome core. *Curr Opin Struct Biol* **8**, 33-40 (1998).

27. Brower-Toland, B.D. et al. Mechanical disruption of individual nucleosomes reveals a reversible multistage release of DNA. *Proc Natl Acad Sci U S A* **99**, 1960-5 (2002).

28. Neuman, K. C. and S. M. Block, Optical trapping. *Rev Sci Instrum* **75**(9): 2787-809 (2004).

29. Wang, M. D., H. Yin, R. Landick, J. Gelles and S. M. Block, Stretching DNA with optical tweezers. *Biophys J* **72**(3): 1335-46 (1997).

30. Mihardja, S., Spakowitz, A.J., Zhang, Y. & Bustamante, C. Effect of force on mononucleosomal dynamics. *Proc Natl Acad Sci U S A* **103**, 15871-6 (2006).

31. Kulic, I.M. & Schiessel, H. DNA spools under tension. *Phys Rev Lett* **92**, 228101 (2004).

32. Sakaue, T. & Lowen, H. Unwrapping of DNA-protein complexes under external stretching. *Phys Rev E Stat Nonlin Soft Matter Phys* **70**, 021801 (2004).

# Chapter 2:
# Optical Trapping and
# the Mechanical Separation of DNA

***Theory of operation for a single optical trap***

Optical tweezers are capable of manipulating nanometer and micrometer-sized dielectric particles by exerting extremely small forces (~ piconewton) via a highly focused laser beam[1,2,3]. The beam is typically focused by sending it through a microscope objective. The narrowest point of the focused beam, the beam waist, contains a very strong electric field gradient. Dielectric particles are attracted along the gradient to the center of the beam where the electric field is strongest. In addition to the gradient force, there is a scattering force along the direction of beam propagation due to the backscattering of light from the trapped particle. This displaces the particle slightly downstream relative to the beam waist, as shown in Figure 2.1.

Optical traps are very sensitive instruments and are capable of the manipulation and detection of sub-nanometer displacements for sub-micrometer dielectric particles. For this reason, they are often used to manipulate and study single molecules by interacting with a bead that has been attached to that molecule.

For quantitative scientific measurements, most optical traps are operated in such a way that the dielectric particle rarely moves far from the trap center. The reason for this is that the force applied to the particle is linear with respect to its displacement from the center of the trap as long as the displacement is small. In this way, an optical trap can be compared to a simple spring, which follows Hooke's law, as indicated in Figure 2.1. A proper explanation of optical trapping behavior depends upon the size of the trapped particle relative to the wavelength of light used to trap it. In cases where the dimensions of the particle are much greater than the wavelength, a simple ray optics treatment is sufficient. If the wavelength of light far exceeds the particle dimensions, the particles can be treated as electric dipoles in an electric field. For optical trapping

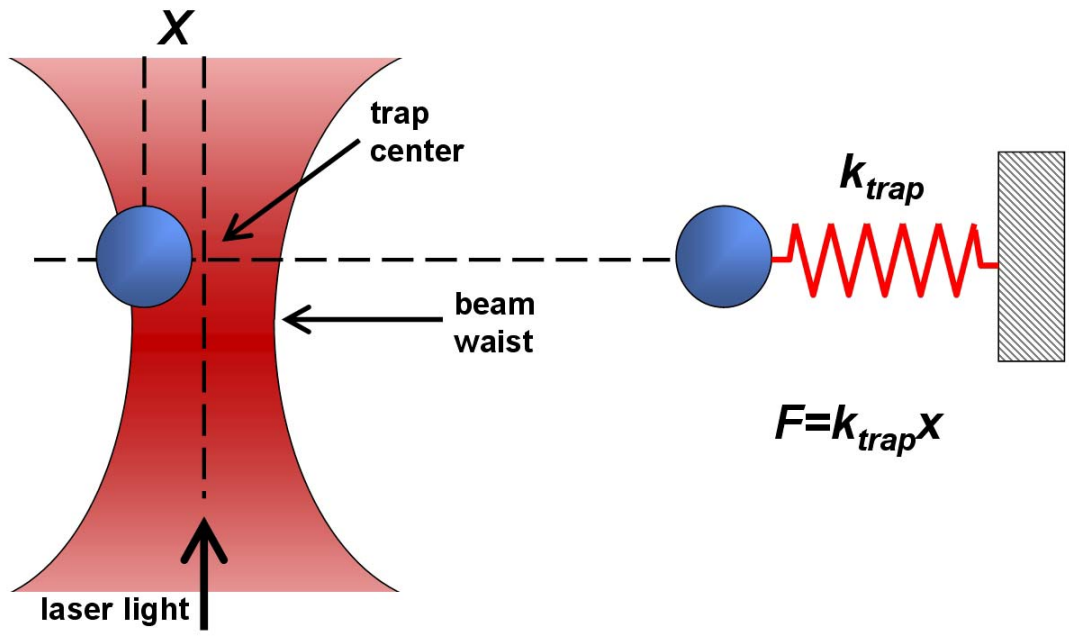


**Figure 2.1 An optical trap as a Hookean spring.** As derived in the main text, the force applied to a small dielectric particle by a focused laser beam is proportional to the gradient of the intensity of the beam, as described in Equation 2.11. Our apparatus uses a Gaussian beam ($TEM_{00}$ mode) profile intensity, ensuring that the force applied to a trapped microsphere within ~ 200 nm region on either side of the center of the beam is linear and may be treated as a Hookean spring. In practice, during the calibration procedure, we fit the beam deflection observed versus a known translation of microsphere to a seventh order polynomial, which both increases the useable deflection range of our instrument and improves its position and force detection accuracy.

of dielectric objects of dimensions within an order of magnitude of the trapping beam wavelength, the only accurate models involve the treatment of either time dependent or time harmonic Maxwell equations using appropriate boundary conditions.

In cases where the diameter of a trapped particle is significantly greater than the wavelength of light, the trapping phenomenon can be explained using ray optics. As shown in Figure 2.2, individual rays of light emitted from the laser will be refracted as it enters and exits the dielectric bead. As a result, the ray will exit in a direction different from which it originated. Since light has momentum, this change in direction corresponds to a momentum change on the particle.

Most optical traps operate with a Gaussian beam ($TEM_{00}$ mode) profile intensity. In this case, if the particle is displaced from the center of the beam, as in Figure 2.1, the particle has a net force returning it to the center of the trap because more intense beams impart a larger momentum change towards the center of the trap than less intense beams, which impart a smaller momentum change away from the trap center. The net change in momentum, or force, returns the particle to the trap center.

If the particle is located at the center of the beam, then individual rays of light are refracting through the particle symmetrically, resulting in no net lateral force. The net force in this case is long the axial direction of the trap, which cancels out the scattering force of the laser light. The cancellation of this axial gradient force with the scattering force is what causes the bead to be stably trapped slightly downstream of the beam waist.

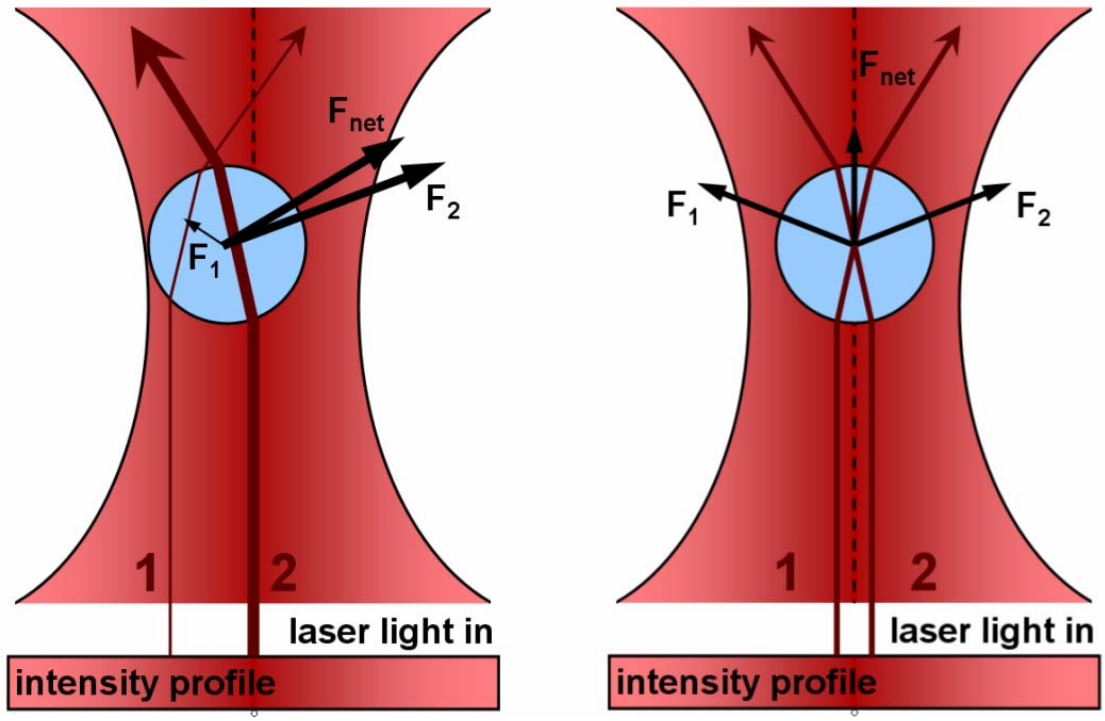


**Figure 2.2 A ray optics approach to explaining optical tweezers.** Tracing the deflection of individual beams of light for a focused beam with a Gaussian intensity profile yields an intuitive heuristic explanation of the operating principle of an optical trap. When a dielectric microsphere is displaces from the trap center, high intensity rays from the center of the trap are deflected away from the center, imparting a momentum to the trapped particle toward the trap center. For each deflection of this type, a corresponding ray of lower intensity is deflected toward the center of the trap, imparting a momentum to the bead away from the trap center. On net balance, a microsphere displaced from the trap center will have a net momentum that returns it toward the trap center. A dielectric microsphere that is located at the exact center of the trap will have no net momentum applied to it because for every ray that imparts a momentum in one direction, a ray of equal intensity imparts momentum in the opposite direction.

In cases where the diameter of a trapped particle is significantly smaller than the wavelength of light, the conditions for Rayleigh scattering are satisfied and the particle can be treated as a point dipole in an inhomogeneous electromagnetic field. The force applied on a single charge in an electromagnetic field is the Lorentz force,

$$\mathbf{F}_1 = q\left(\mathbf{E}_1 + \frac{d\,\mathbf{x}_1}{dt} \times \mathbf{B}\right). \tag{2.1}$$

The force on the dipole can be calculated by substituting two terms for the electric field into the equation above, one for each charge. The polarization of a dipole is $\boldsymbol{p = qd}$, where $\boldsymbol{d}$ is the distance between the two charges. For a point dipole, the distance is infinitesimal, $\boldsymbol{x_1 - x_2}$. Taking into account that the two charges have opposite signs, the force takes the form:

$$\mathbf{F} = q\left(\mathbf{E}_1(x,y,z) - \mathbf{E}_2(x,y,z) + \frac{d(\mathbf{x}_1 - \mathbf{x}_2)}{dt} \times \mathbf{B}\right) \tag{2.2}$$

$$\mathbf{F} = q\left(\mathbf{E}_1(x,y,z) + ((\mathbf{x}_1 - \mathbf{x}_2)\cdot\nabla)\mathbf{E} - \mathbf{E}_1(x,y,z) + \frac{d(\mathbf{x}_1 - \mathbf{x}_2)}{dt} \times \mathbf{B}\right). \tag{2.3}$$

Notice that the $\mathbf{E}_1$ cancel out. Multiplying through by the charge, $q$, converts position, $\mathbf{x}$, into polarization, $\mathbf{p}$.

$$\mathbf{F} = (\mathbf{p}\cdot\nabla)\mathbf{E} + \frac{d\,\mathbf{p}}{dt} \times \mathbf{B} \tag{2.4}$$

$$\mathbf{F} = \alpha\left[(\mathbf{E}\cdot\nabla)\mathbf{E} + \frac{d\,\mathbf{E}}{dt} \times \mathbf{B}\right], \tag{2.5}$$

where in the second equality, it has been assumed that the dielectric particle is linear (i.e. $\mathbf{p} = \alpha\,\mathbf{E}$). In the final steps, two equalities will be used: (1) a vector analysis equality; (2) one of Maxwell's equations:

1. $$(\mathbf{E}\cdot\nabla)\mathbf{E} = \nabla\left(\frac{1}{2}E^2\right) - \mathbf{E}\times(\nabla\times\mathbf{E}) \tag{2.6}$$

2. $$\nabla\times\mathbf{E} = -\frac{\partial\mathbf{B}}{\partial t} \tag{2.7}$$

First, the vector equality will be inserted for the first term in the force equation above. Maxwell's equation will be substituted in for the second term in the vector equality. Then the two terms which contain time derivatives can be combined into a single term.

$$\mathbf{F} = \alpha\left[\frac{1}{2}\nabla E^2 - \mathbf{E}\times\left(\nabla\times\mathbf{E}\right) + \frac{d\,\mathbf{E}}{dt}\times\mathbf{B}\right] \tag{2.8}$$

$$\mathbf{F} = \alpha\left[\frac{1}{2}\nabla E^2 - \mathbf{E}\times\left(-\frac{d\,\mathbf{B}}{dt}\right) + \frac{d\,\mathbf{E}}{dt}\times\mathbf{B}\right] \tag{2.9}$$

$$\mathbf{F} = \alpha\left(\frac{1}{2}\nabla E^2 + \frac{d}{dt}\left(\mathbf{E}\times\mathbf{B}\right)\right). \tag{2.10}$$

The second term in the last equality is the time derivative of a quantity that is related through a multiplicative constant to the Poynting vector, which describes the power per unit area passing through a surface. Since the power of the laser is constant when sampling over frequencies much shorter than the frequency of the laser's light ~ $10^{14}$ Hz, the derivative of this term averages to zero and the force can be written as

$$\mathbf{F} = \frac{1}{2}\alpha\nabla E^2 . \tag{2.11}$$

The square of the magnitude of the electric field is equal to the intensity of the beam as a function of position. Therefore, the result indicates that the force on the dielectric particle, when treated as a point dipole, is proportional to the gradient along the intensity of the beam. In other words, the gradient force described here tends to attract the particle to the region of highest intensity. In reality, the scattering force of the light works against the gradient force in the axial direction of the trap, resulting in an equilibrium position that is displaced slightly downstream of the intensity maximum. Under the Rayleigh approximation, the scattering force can be written as (Harada, 1996)

$$\mathbf{F}_{\mathbf{scat}}\left(\mathbf{r}\right) = \frac{k^4\alpha^2}{6\pi\pi c^3 {\varepsilon_0}^2} I\left(\mathbf{r}\right)\hat{\mathbf{z}} \tag{2.12}$$

***Layout of our single beam optical trapping apparatus***

Our single beam optical trapping instrument has a very simple design, containing the minimal set of experimental components required for the operation of a high precision instrument of its kind. It has been described in detail elsewhere[4]. A simplified schematic is represented in Figure 2.3. A 1064 nm laser is expanded and incident on the back focal plane of an oil-immersion microscope objective that is mounted in a modified Nikon inverted microscope. Slightly overfilling the objective aperture ensures maximal intensity gradient along the axis of propagation, which is critical for overcoming the scattering force. Forward scattered light is collected by an oil-immersion condenser lens and imaged onto a quadrant photodiode (QPD). Displacements of trapped polystyrene spheres impart a deflection to the forward scattered light, are captured as a differential voltage signal at the QPD and later converted to force and extension measurements. The laser intensity is adjusted by modulating the voltage amplitude applied to an acoustic optical deflector (AOD) placed between the laser aperture and the beam expander. Samples are manipulated manually via a micro-stage or via a high precision 1D piezo stage.

***Layout of our dual beam optical trapping apparatus***

The basic operating principle underlying a dual beam optical trap is similar to that of a single trap apparatus, except that two traps are generated by splitting the incident laser beam through a polarizing beam splitting cube (Figure 2.4). In our apparatus, described in detail elsewhere[5], the absolute position of one of the beams is fixed ("fixed beam"). The other ("steered beam") is incident on a tip/tilt mirror that can be rotated around two perpendicular axes. The rotation is mapped to the back focal plane of a water-immersion microscope objective, converting absolute beam rotation into absolute translation in the sample plane. Forward scattered light from the sample

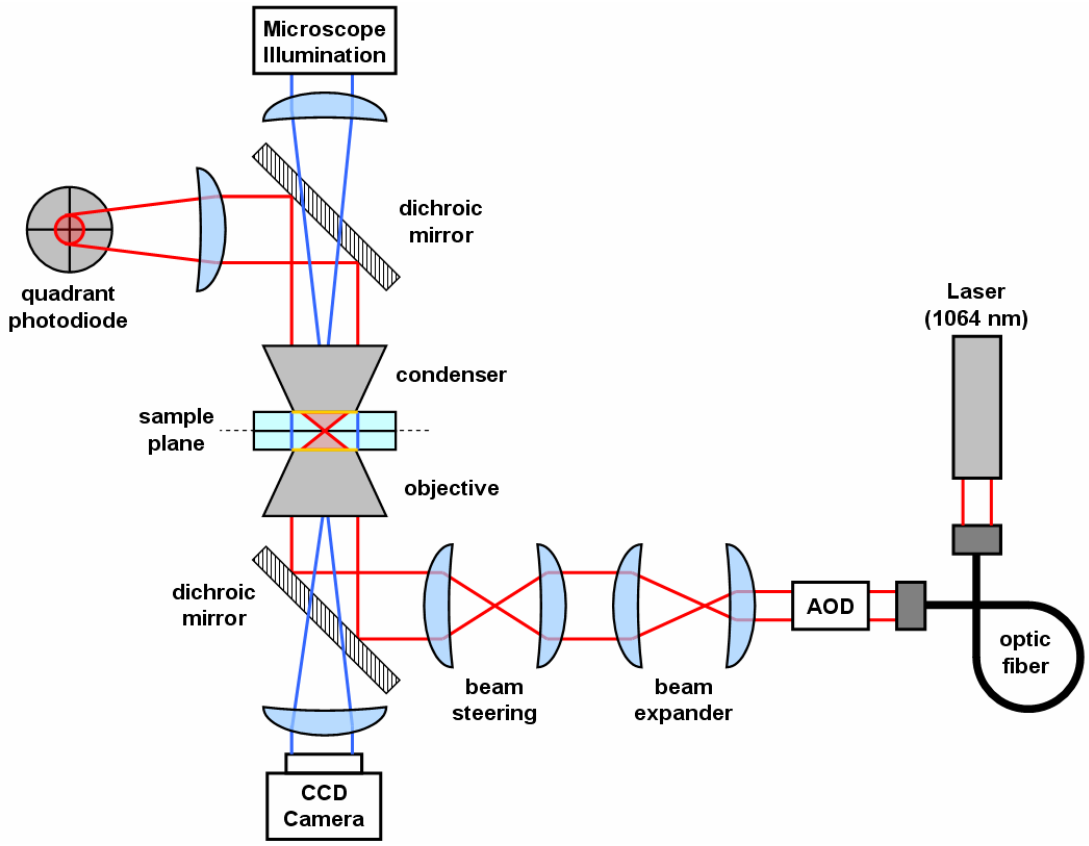


**Figure 2.3 Optical layout of our single beam optical tweezers apparatus.** A 1064 nm continuous wave laser is expanded to slightly overfill the back focal plane of a Nikon oil-immersion objective lens. Forces exerted onto trapped 500 nm diameter polystyrene beads cause deflections in the forward scattered beam, which are detected via a downstream quadrant photodiode. The AOD provides real-time intensity modulation of the beam and the optical fiber reduces laser pointing instability. Illumination is achieved by focusing a Nikon Mercury arc lamp at the back focal plane of the condenser lens, which provides uniform illumination of the sample plane, which is imaged by a CCD camera.

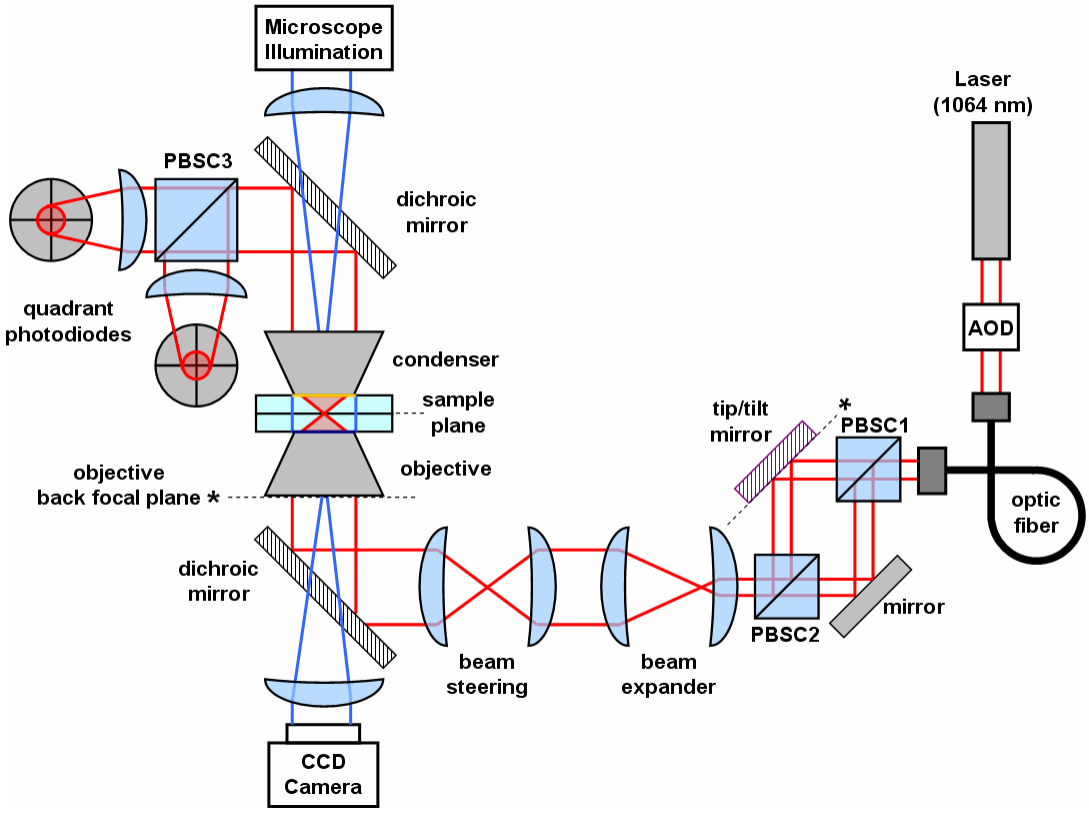


**Figure 2.4 Optical layout of our dual beam optical tweezers apparatus.** This apparatus is similar to the single beam apparatus discussed in Figure 2.3, except: (i) the beam is split into orthogonal polarizations and recombined prior to the beam expander via two polarizing beam splitting cubes (PBSC1 & PBSC2); (ii) one polarization is reflected by a tip/tilt mirror that is mapped to the back focal plane of the objective, converting rotations of the mirror into translations of the beam in the sample plane; (iii) there is a water immersion objective lens instead of an oil immersion lens. The result is a decrease in the trap stiffness in exchange for the ability to trap further into the sample chamber without spherical aberration of the beam; (iv) each beam is separated via polarization (PBSC3) and detected independently on a separate quadrant photodiode.

plane is collected by an oil-immersion condenser lens where the beams are again separated by polarization and the deflection of each beam is measured via its own dedicated QPD. This apparatus is also sensitive to a beads' displacement along the axis of propagation (i.e. "z axis"). As a bead is displaced axially from the trap center, there is interference between the forward scattered light and the un-scattered light. The variable constructive or destructive interference is known as the Guoy phase shift[6] and is normalized by the input laser intensity, measured prior to beam propagation into the microscope objective.

***The unzipping assay***

The mechanical separation of the two strands of dsDNA has been studied both theoretically and experimentally[7,8,9]. Our lab has adapted this technique as a powerful means to measure the location and affinity of DNA bound proteins[10,11]. Briefly, our lab uses an optical trap to apply a force perpendicular to the contour length of a single dsDNA molecule and across the first paired base (Figure 2.5a). Application of force along the DNA strands stores energy in its extension which destabilizes the next sequentially paired base (Figure 2.5a). Thermal fluctuations mean that the unzipping fork explores a wide range of base pair positions at very high frequency, so the measured fork position is an average. For that reason, the force at which dsDNA unzips is ~ 15 pN, but varies depending upon the local sequence composition: regions containing relatively higher GC sequence content yield measured forces that are modestly higher than their AT rich counterparts. When a protein is bound to DNA, the unzipping fork encounters a significant barrier to advancement. In response, the force along the ssDNA is increased well above the baseline through a very narrow range of fork positions. A dwell time histogram of the fork position reveals the location and strength of the protein-DNA interaction in question.

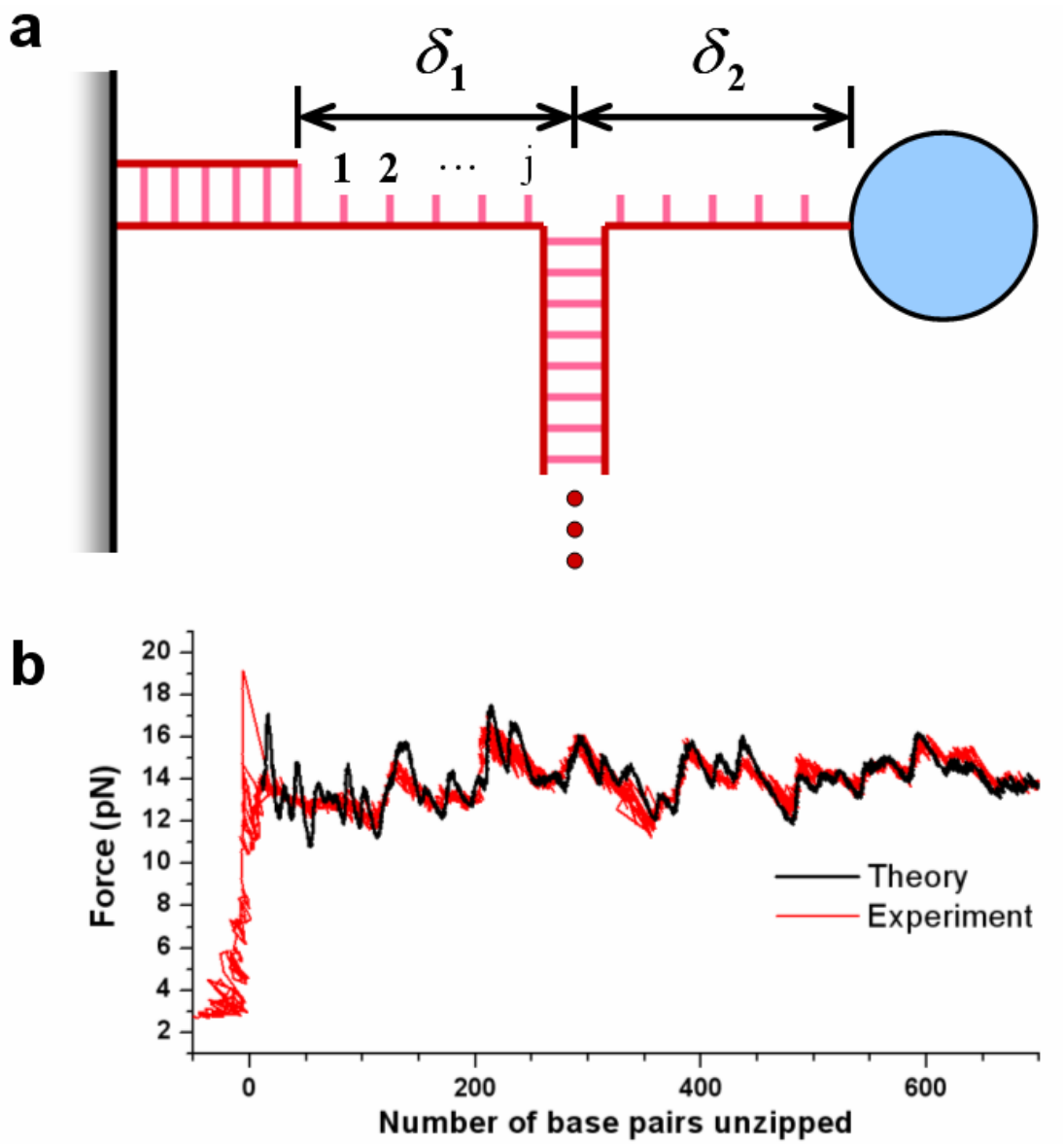


**Figure 2.5 A theoretical description of the unzipping fork.** (a) The advancement of the unzipping fork is a competition between the energy stored in the extension of double and single stranded DNA between the trapped bead and the surface of the cover slip and the sum of the potential energy from all of the disrupted base pairs up to the current fork position. (b) A representative experimental trace (red) aligns very well with the theoretical prediction (black) after adjustment of the trap height and data alignment (as described in the text).

Previously, this technique has demonstrated an accuracy of ~ 25 bp, a precision of ~ 30 bp and a resolution of ~ 3 bp for the detection of simple restriction enzyme binding sites of ~ 12 bp in extent[10]. More recent work has applied it to the nucleosome and has estimated the distribution of a population of nucleosomes at ~ 3 bp[12]. As demonstrated in Chapter 3, I have increased the precision and accuracy of this technique to measure single interaction sites with a precision and accuracy of nearly 1 bp and a resolution of better than 1 bp. This has allowed for the precise measurement of the individual histone-DNA interactions that are densely packed within the nucleosome.

In Chapter 4, I demonstrate that this technique has been extended so that single dsDNA molecules may be unzipped while the unzipping segment is simultaneously held under tension. We expect that this novel single molecule assay will open up a wide range of new possibilities for study, some of which will be suggested later. Furthermore, unzipping under tension is one of few aspects of mechanical strand separation that has not yet been addressed theoretically – most likely, because it has not yet been demonstrated experimentally until now.

***A theoretical description of the unzipping fork***

The mechanical strand separation of dsDNA has been studied extensively theoretically. We use an equilibrium statistical mechanics theoretical description of the unzipping fork similar to what has been described elsewhere[13]. Briefly, whether or not an unzipping fork advances forward on a naked dsDNA template depends upon the competition of (a) the potential energy stored as the extension of dsDNA and ssDNA in the arms (encouraging fork advancement) versus (b) the interaction affinity of

undisrupted base pairs (discouraging fork advancement) and (c) the potential energy of disrupted base pairs (encouraging reannealing of the separated strands) (Figure 2.5a).

The thermal average of an observable, $\langle A \rangle$, is calculated according to

$$\langle A \rangle = \frac{\sum_{j,\delta_1,\delta_2} A(j,\delta_1,\delta_2) e^{-E_{tot}(j,\delta_1,\delta_2)/kT}}{\sum_{j,\delta_1,\delta_2} e^{-E_{tot}(j,\delta_1,\delta_2)/kT}}, \quad (2.13)$$

where the total energy in our case given by

$$E_{tot} = E_{DNA}(j) + E_{ext}(j,\delta_1,\delta_2) + E_{trap}(\delta_1 + \delta_2). \quad (2.14)$$

For our experiments, a theory trace is generated for the unzipping segment under consideration and each dataset is aligned with it. A comparison of the theoretical prediction with properly treated experimental data is shown in Figure 2.5b.

***Data treatment – determination of trap height***

The interactions between histones and DNA in a nucleosome are very densely spaced. The accuracy and precision of our unzipping data analysis method had to be increased significantly in order to confidently identify them all. Two important data treatment procedures are described here.

Unzipping DNA using our single beam optical trap is performed in the XZ plane. The X component of DNA extension is known through the use of a high precision X piezo stage. However, the lack of Z piezo control results in uncertainty in the Z component. Historically, part of our calibration procedure has been to measure the height of the trap center relative to the surface of the cover slip and that value has been used to convert the XY bead displacements into the extension of DNA in the XZ plane (described in detail elsewhere). But in reality, the height of the trap center changes

every time a user refocuses the microscope objective, which occurs before the collection of data for every molecule. Therefore, there is an uncertainty on the order of ~ 100 nm from trace to trace which effects the unzipping calculation significantly for experiments where high precision is required.

To overcome this obstacle, I've implemented a technique where the trap height can be estimated prior to the calculation of unzipping fork position. As shown in the Figure 2.5b, prior to strand separation, the force applied to the unzipping fork rises from 0 pN to ~ 15 pN. During that time, the dsDNA anchor undergoes a typical force-extension stretch curve and no base pairs are unzipped. Since the contour length of the DNA anchor segment is known, the trap height may be estimated by fitting the initial dsDNA stretch curve to its theoretically predicted behavior. After estimating the trap height in this way, the initial rise in force, when plotted against the number of base pairs unzipped, ought to be vertical at ~ 0 bp, as shown in Figure 2.5b.

***Data treatment – alignment of data to theory***

After tweaking the trap height, the raw extension data is converted and the fork position is calculated using a procedure described elsewhere[4]. After a direct conversion, it is the unzipping data may be both shifted and slightly elongated compared to the theoretical prediction (Figure 2.6a). We attribute this discrepancy, respectively, to slight errors in the estimation of the tethering attachment point to the surface of the cover slip or stage drift along the Z dimension (due primarily to shifting of the oil between the cover slip and the oil immersion objective lens) resulting in a cumulative error in the trap height measurement over the course of an unzipping trace. We correct for these errors by resampling the data along the X axis ("number of base pairs unzipped") and cross correlating each dataset separately against a theoretical

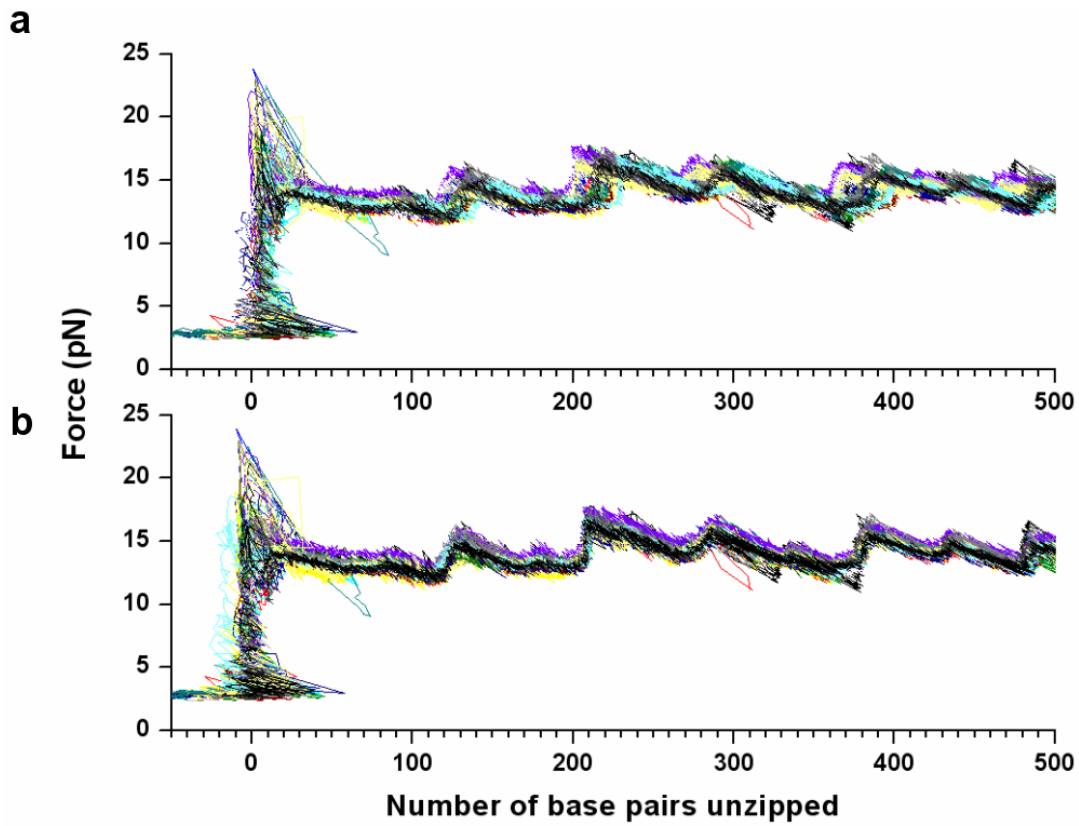


**Figure 2.6 Comparison of naked DNA unzipping data before and after alignment.** (a) Several naked DNA unzipping curves (N = 30) shown after calculation of fork location in base pairs unzipped. Trap height optimization has been applied, as evidenced by the consistently vertical force observed at zero base pairs unzipped. Notice that different datasets do not align particularly well, especially at unzipping fork locations further downstream. (b) The same unzipping curves (N = 30) after alignment with the theoretical prediction. Here, the data overlaps much better over the complete length of the template under observation. This technique has been shown to work on templates as long as 4 kbp without a noticeable reduction in its alignment precision and accuracy (data not shown).

curve generated for the DNA sequence in question. The dataset is shifted and/or elongated along the X axis and a single shift-stretch pair is chosen and applied to the data using a multi-layered SIMPLEX algorithm. Through the use of this algorithm, the accuracy and precision of determining a single protein-DNA interaction location improves from ~ 25 and ~ 30 bp to nearly 1 bp each, respectively (Figure 2.6b).

In the presence of the nucleosome, nearly 150 bp of DNA are occluded. This severely interferes with the alignment process because the theoretical prediction is valid for the unzipping of naked dsDNA only. Optimal selection of which shift and stretch parameters to apply to each dataset are best ensured by correlating over the longest extent of naked dsDNA unzipping data possible. Therefore, software has been written in LabView that allows the user to manually select the region of observe nucleosome interactions, which is then excluded from correlation. In this way, unzipping data for naked DNA both before and after the nucleosome position is included in the correlation and this has been shown to improve the selection of the shift and stretch parameters on datasets containing nucleosomes considerably.

REFERENCES


1. Ashkin A., Optical trapping and manipulation of neutral particles using lasers. *Proc Natl Acad Sci U S A* **94**(10):4853-4860.
2. Ashkin A, Dziedzic JM, Bjorkholm JE and Chu S, Observation of a single-beam gradient force optical trap for dielectric particles. *Opt Lett.* **11**(5): 288.
3. Neuman, K. C. and S. M. Block, Optical trapping. *Rev Sci Instrum* **75**(9): 2787-809 (2004).
4. Shundrovsky A, Single molecule studies of sequence-dependent transcription pausing. *Cornell University PhD Thesis* (2004).
5. Smith B, Measuring the physical step-size of bacteriophage T7 DNA helicase with a dual optical trap. *Cornell University PhD Thesis* (2011).
6. Dreyer, J.K., K. Berg-Sørensen, and L. Oddershede. Improved Axial Position Detection in Optical Tweezers Measurements. *Appl. Optics.* **43**(10):1991-1996 (2004).
7. Essevaz-Roulet B, Bockelmann U and Heslot F, Mechanical separation of the complementary strands of DNA. *Proc Natl Acad Sci U S A* **94**(22): 11935-40 (1997).
8. Bockelmann U, Thomen P, Essevaz-Roulet B, Viasnoff V and Heslot F, Unzipping DNA with optical tweezers: high sequence sensitivity and force flips. *Biophys J* **82**(3): 1537-53 (2002).
9. Singh AR, Giri D and Kumar S, Force induced melting of the constrained DNA, *J Chem Phys* **132**(23): 235105 (2010).
10. Koch, S.J., Shundrovsky, A., Jantzen, B.C. & Wang, M.D. Probing protein-DNA interactions by unzipping a single DNA double helix. *Biophys J* **83**, 1098-105 (2002).

11. Koch SJ and Wang MD, Dynamic force spectroscopy of protein-DNA interactions by unzipping DNA. *Phys Rev Lett* **91**(2):028103 (2003).

12. Shundrovsky, A., Smith, C.L., Lis, J.T., Peterson, C.L. & Wang, M.D. Probing SWI/SNF remodeling of the nucleosome by unzipping single DNA molecules. *Nat Struct Mol Biol* **13**, 549-54 (2006).

13. Bockelmann U, Essevaz-Roulet and Heslot F, DNA strand separation studied by single molecule force measurements. *Phys Rev E* **58**(2):2386 (1998).

# Chapter 3:
# High-Resolution Dynamic Mapping of Histone-DNA Interactions in a Nucleosome

* Portions reprinted from Nature Structural and Molecular Biology (NSMB) Journal, Volume 16(2): pages 124-129, Copyright 2009, with permission from Nature Publishing Group.

***Introduction***

The nucleosome is the fundamental repeating unit of eukaryotic chromatin, consisting of ~147 bp of DNA wrapped ~1.7 times around a histone octamer [1]. Nucleosomes must be stable and yet dynamic structures, both maintaining eukaryotic DNA in a condensed state and also permitting regulated access to genetic information contained therein. During many important cellular processes, DNA-binding proteins must gain access to specific genomic regions that are occluded by nucleosomes. In particular, in vitro studies show that RNA polymerase slows down, pauses, or stalls upon encountering a nucleosome [2-7]. The resistance that RNA polymerase encounters when transcribing a chromatin template should be largely dictated by both the strengths and locations of histone-DNA interactions in the nucleosome. Therefore a detailed map of these interactions would lay an important foundation for understanding the structural details of eukaryotic transcription and how gene expression may be regulated by histone modifications, DNA sequence, and nucleosome remodeling.

Analysis of the nucleosome crystal structure indicates that histone-DNA interactions are not uniform along the DNA [1,8]; however, experimental determination of this interaction map has proven to be challenging and is still largely controversial. Although it is well established that the overall stability of a nucleosome depends on its constituent DNA sequence and histone modifications [9-11], the way in which the specific interactions in a nucleosome lead to this stability is less well understood. The mechanical nature of this problem makes it ideally suited for investigation by single molecule manipulation approaches [12-19]. Previously, we have stretched single DNA molecules of chromatin and obtained data on the *relative* locations of strong histone-DNA interactions [14,17]. These data indicate the presence of three regions of strong interactions, consistent with those suggested by counting the number of apparent

histone-DNA contacts seen in the nucleosome crystal structure [20]. However, subsequent single molecule stretching experiments challenged this interpretation and suggested that force signatures from stretching experiments can be attributed to the rotation of the spool geometry of the nucleosome rather than regions of strong histone-DNA interactions [21]. These studies favor a model in which histone-DNA interactions are uniform along the DNA [22,23]. The controversy arose because stretching experiments can not readily separate contributions from geometry and interaction strengths nor can they quantitatively assay interaction strengths near the dyad. Recently, we have developed a method to sequentially determine the *absolute* locations of histone-DNA interactions by mechanically unzipping a DNA molecule containing a nucleosome [16]. However, the precision of that method was insufficient to map out all of the densely packed histone-DNA interactions in a nucleosome. In the current work, using an improved unzipping method, we have mapped the locations of the interactions to near bp accuracy along the DNA sequence and quantitatively assayed the strengths of these interactions. The ability to sequentially map out the histone-DNA interactions along nucleosomal DNA demonstrated in this work should unambiguously resolve the controversy on the distribution of these interactions in the nucleosome. The histone-DNA interaction map, together with mechanical invasion experiments, provide a simple explanation of the RNA polymerase pausing pattern within a nucleosome and makes testable predictions on the fate of histones upon transcription.

***Precision mapping of interactions to near bp***

The basic experimental configuration is sketched in Figures 3.1 and 3.3a (see also Methods). A DNA molecule containing a single nucleosome uniquely positioned at a 601 nucleosome positioning sequence [24] was attached to the surface of a microscope

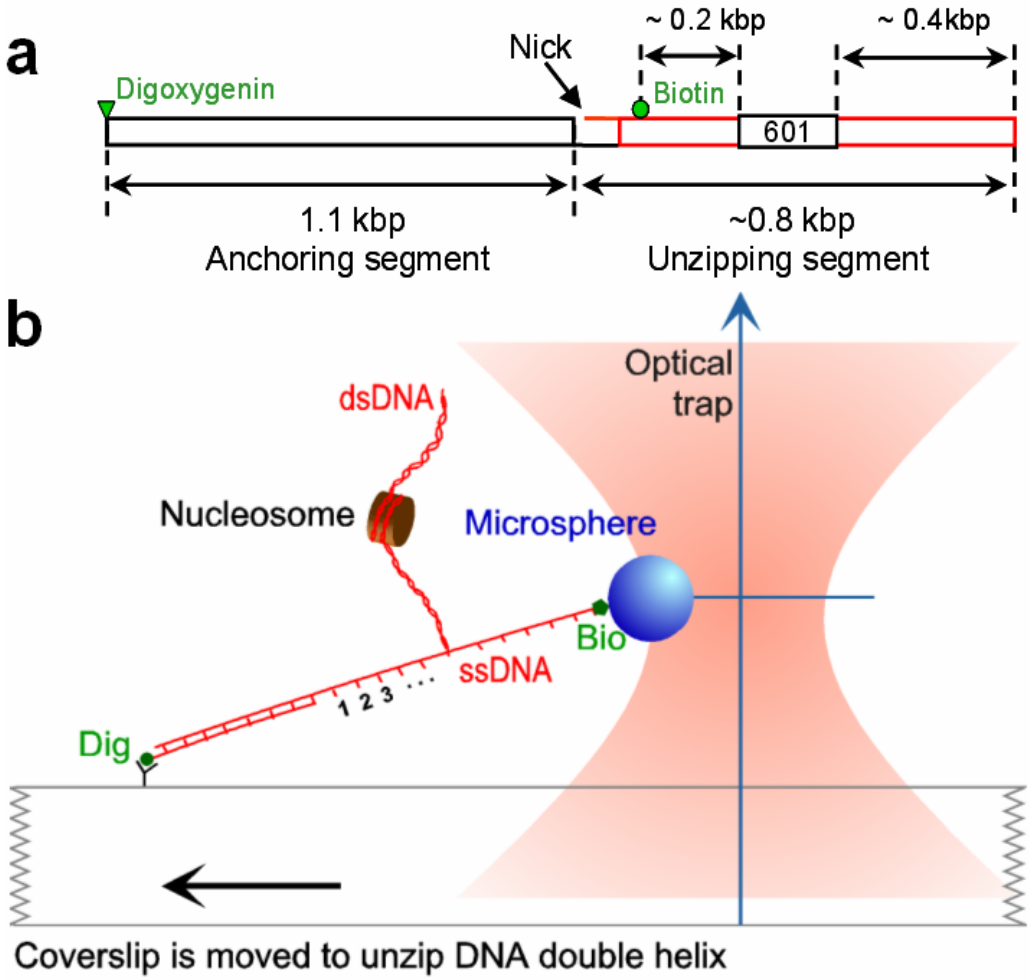


**Figure 3.1. Experimental configuration (adapted from Shundrovky et al., 2006).** a, DNA template for single molecule experiments consisted of two parts, separated by a nick in one DNA strand: (1) dig-labeled anchoring segment always remained double stranded and (2) biotin-labeled unzipping segment had its two DNA strands separated (unzipped) during experiments. The unzipping segment contained a single strong 601 nucleosome positioning sequence (601). **b,** Nucleosomal template was suspended between the glass coverslip surface and a microsphere via a digoxigenin-antidigoxigenin linkage at the coverslip and a biotin-streptavidin linkage at the microsphere. An optical trap was used to apply a force necessary to unzip through the DNA and nucleosome as the coverslip was moved away from the trapped microsphere.

coverslip via one of its strands and to the surface of a microsphere held in an optical trap via the other strand [16]. As the coverslip was moved away from the trapped microsphere, dsDNA was sequentially converted to ssDNA upon base pair separation. As the unzipping fork progressed through the nucleosome, it encountered resistance from histone-DNA interactions at well-defined locations and, because these interactions require dsDNA, they were sequentially disrupted. The magnitude of resistance should strongly correlate with histone-DNA affinity, and thus a histone-DNA interaction map was generated along the DNA. We showed that this technique achieved a resolution of better than 1 bp (Figure 3.2a-c). Its accuracy and precision of determining the absolute sequence position of an interaction were both ~ 1.5 bp (Figure 3.2b).

***Mapping the strengths of histone-DNA interactions in a nucleosome***

To quantitatively assay the strengths of the histone-DNA interactions, we unzipped through individual nucleosomal DNA molecules with a constant unzipping force of ~28 pN (see Methods). Under a force clamp [25], the dwell times at different sequence positions measure the strengths of interactions at those positions, provided that disruption of each interaction follows a similar energy landscape. Thus this method allows direct mapping of the strengths of interactions. Figure 3.3b shows example traces for unzipping DNA through a nucleosome under a constant force (for additional traces, see Figure 3.4). DNA molecules were unzipped from both directions along the DNA (referred to here as "forward" and "reverse") (see Methods and Figure 3.4). In both cases, the unzipping fork did not move through the nucleosomal DNA at a constant rate but instead dwelled at specific locations within the nucleosome, indicating the presence of strong interactions. In particular, these traces revealed that

**Figure 3.2. Unzipping accuracy, precision, and resolution.** To determine the ability of this technique to locate the absolute position of an interaction, naked DNA templates capped with hairpins at distal ends were fully unzipped. The hairpins acted as strong interactions of known locations. **a**, Configuration of three hairpin-capped DNA templates. The position of the 601 sequence relative to the hairpin is also indicated. **b**, Accuracy and precision. DNA molecules were unzipped with a force loading clamp (8 pN/s) for the three templates: 258 bp (black, N = 21), 437 bp (red, N = 27) and 595 bp (green, N = 33). For each trace, a histogram was generated from data points in the vertically rising section only and the hairpin location was taken as its mean. Histograms of these locations are shown along with the corresponding accuracy and precision. The accuracy for each construct was determined by the difference between the mean of the histogram and the expected value (dashed vertical line). The precision was determined by the standard deviation of the histogram. **c,** The resolution for each construct was determined by the average standard error in the measured position from individual traces. This was a function of the signal average time. Note that all three constructs have similar resolution.

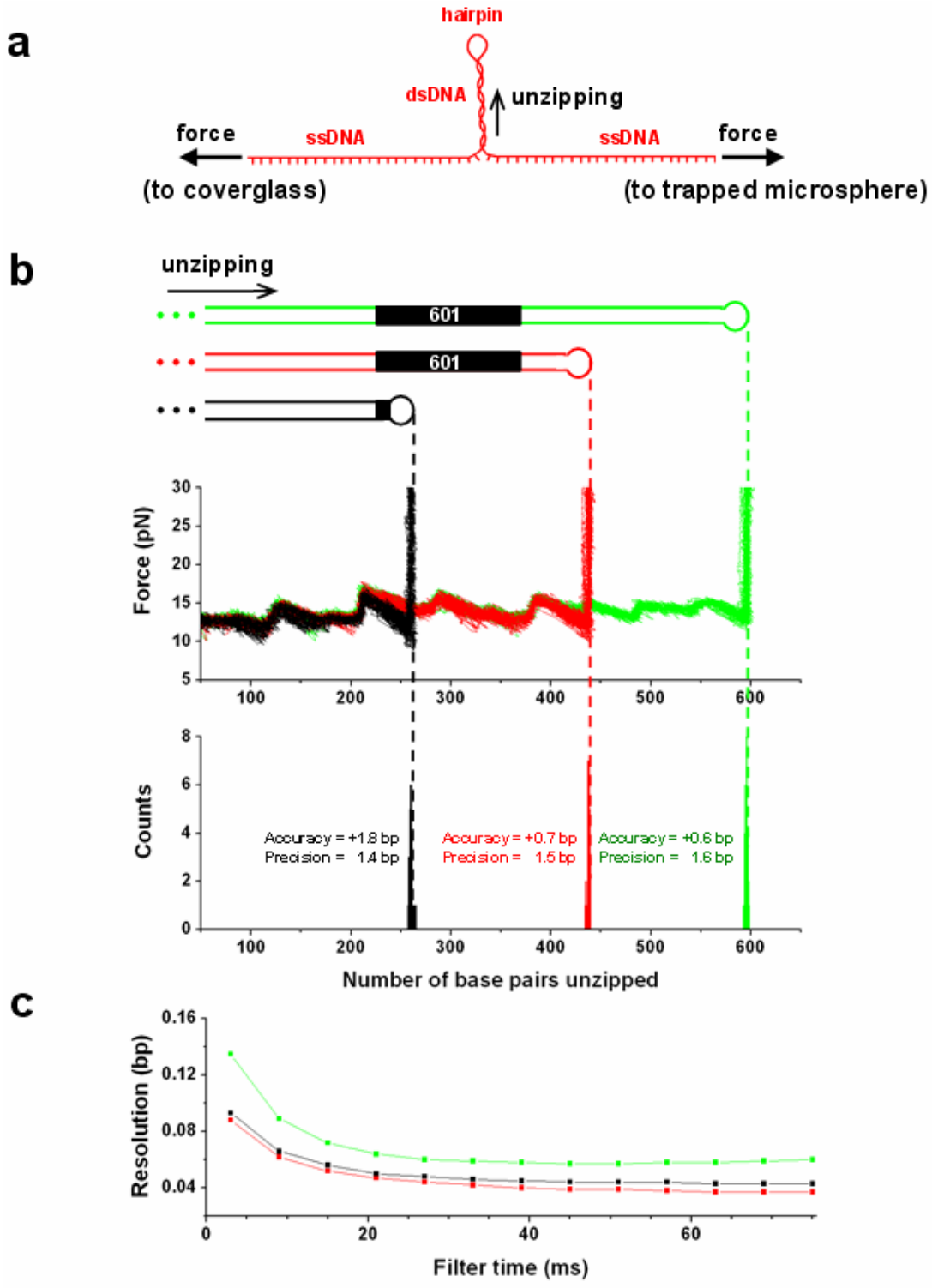
a
hairpin
dsDNA
unzipping
force
ssDNA
ssDNA
force
(to coverglass)
(to trapped microsphere)
b
unzipping
601
601
Force (pN)
Counts
Accuracy = +1.8 bp
Precision = 1.4 bp
Accuracy = +0.7 bp
Precision = 1.5 bp
Accuracy = +0.6 bp
Precision = 1.6 bp
Number of base pairs unzipped
c
Resolution (bp)
Filter time (ms)

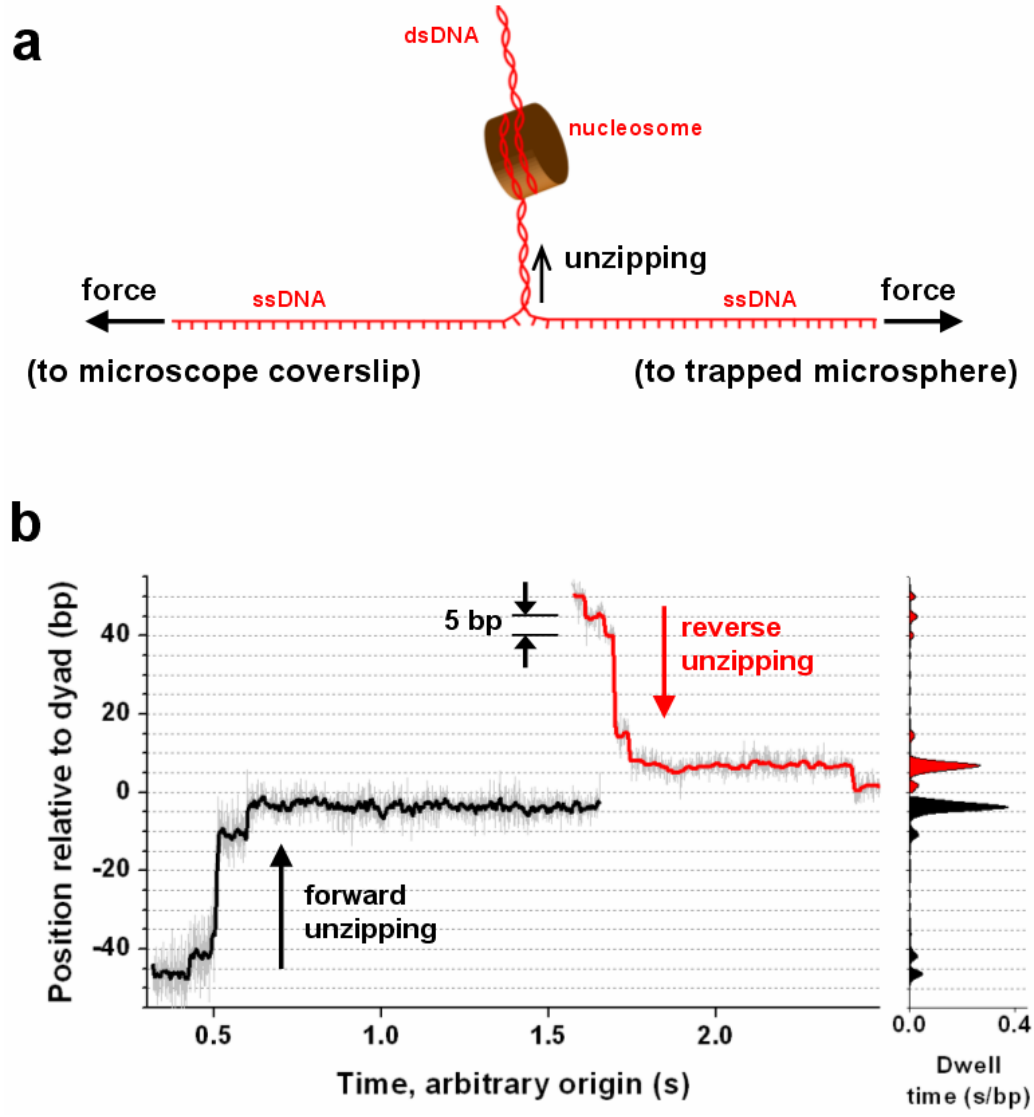


**Figure 3.3. Nucleosome disruptions under a constant unzipping force. a**, Experimental configuration. A DNA molecule was mechanically unzipped through a nucleosome uniquely positioned at a 601 sequence. **b**, Representative traces for unzipping under a constant applied force (~ 28 pN). Two traces are shown: one from forward unzipping (black) and one from reverse unzipping (red). Both traces were low pass filtered from the raw traces (grey) to 60 Hz. The unzipping fork paused at specific locations, which are evident from both the traces (left) and their corresponding dwell time histograms (right)

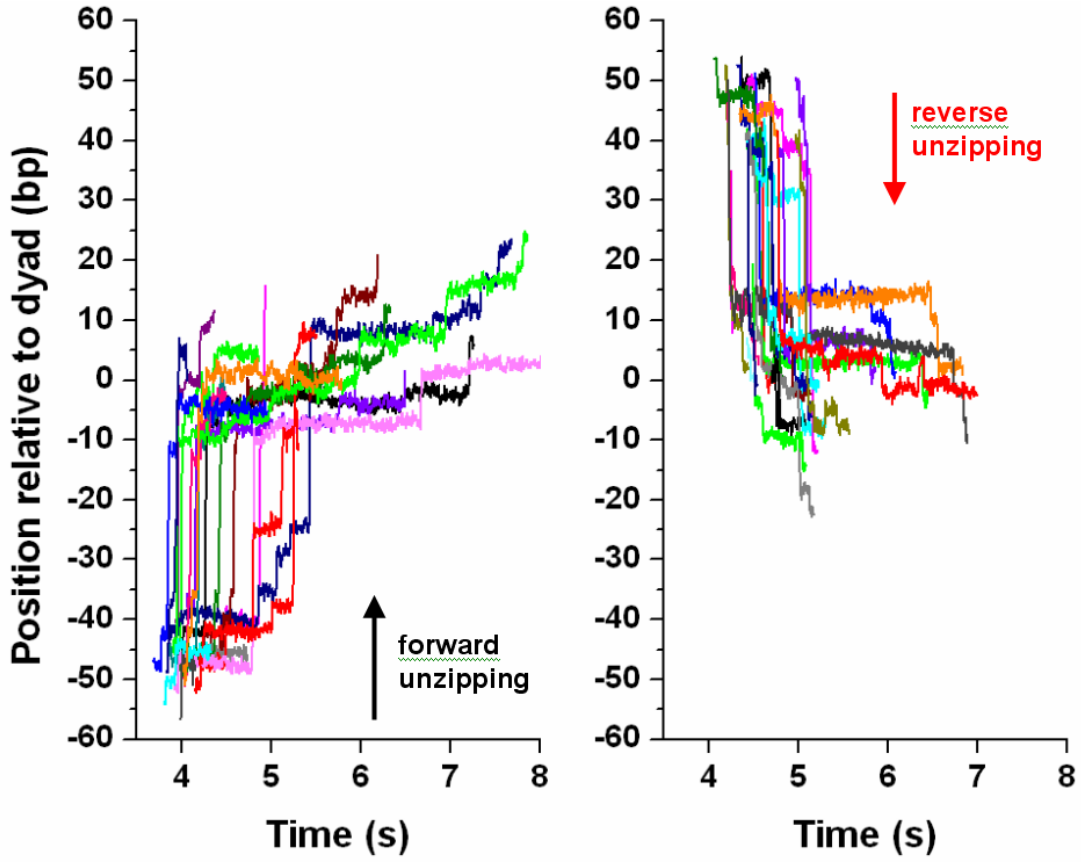


**Figure 3.4. Additional example traces of unzipping through a nucleosome under a constant force.** Experimental conditions are the same as those used in Figure 3.3. Each color represents a single trace.

the fork dwelled with discrete steps spaced by ~ 5 bp and the longest dwell times tended to occur near the dyad.

An interaction map was generated by averaging dwell time histogram measurements from many traces from both forward and reverse unzipping, as shown in Figure 3.5b. Several features are evident from these plots. (1) There are three broad regions of strong interactions: one located at the dyad and two ~ ± 40 bp from the dyad. (2) An ~ 5 bp periodicity occurred within each region of interaction. (3) The interactions near the entry and exit DNA are particularly weak. The unzipping fork did not dwell at a 20 bp region of both entry and exit DNA, indicating that the histones are only loosely bound to the DNA. (4) For unzipping in both the forward and reverse directions, the first two regions of interactions encountered were always detected, but not the last region. This indicates that once the dyad region of interactions was disrupted, the nucleosome became unstable and histones dissociated from the 601 sequence. (5) The total dwell time in the nucleosome was longer in the forward direction compared with that in the reverse direction, indicating nucleosomes were more difficult to disrupt when unzipped in the forward direction, likely reflecting the non-palindromic nature of the 601 sequence.

***Highlighting histone-DNA interactions near entry/exit DNA***

Because the entry and exit DNA regulate the initial invasion of a nucleosome by a motor protein, experiments were carried out starting from a lower unzipping force to specifically detect interactions at those locations and then the force was ramped up to allow complete unzipping through the nucleosomal DNA. We unzipped through nucleosomal DNA molecules under a constant loading rate (8 pN/s), which highlighted the edge of the region first encountered [16] (see Methods). Figure 3.6a

**Figure 3.5. Histone-DNA interaction map within a nucleosome core particle.** **a**, Crystal structure of the nucleosome core particle [1], where dots indicate regions where interactions between DNA and one of the core histones are likely to occur. The two halves of the nucleosome are shown separately for clarity. **b**, A histone-DNA interaction map constructed from the averaged dwell time histograms of the unzipping fork at constant force (~ 28 pN). Individual traces were low-pass filtered to 60 Hz and their dwell time histograms were binned to 1 bp. A total of 27 traces from the forward template and 30 traces from the reverse template were used for the construction. Each peak corresponds to an individual histone-DNA interaction and the heights are indicative of their relative strengths. Three regions of strong interactions are indicated: one located at the dyad (region 2) and two located off-dyad (regions 1 and 3). Colored boxes indicate predictions from the crystal structure where individual histone binding motifs are expected to interact with DNA. The H3 N-terminal αN helices (αN) and the histone loops (L1, L2) and alpha helices (α1) that compose the L1L2 and α1α1 DNA-binding sites, respectively [1], are also indicated.

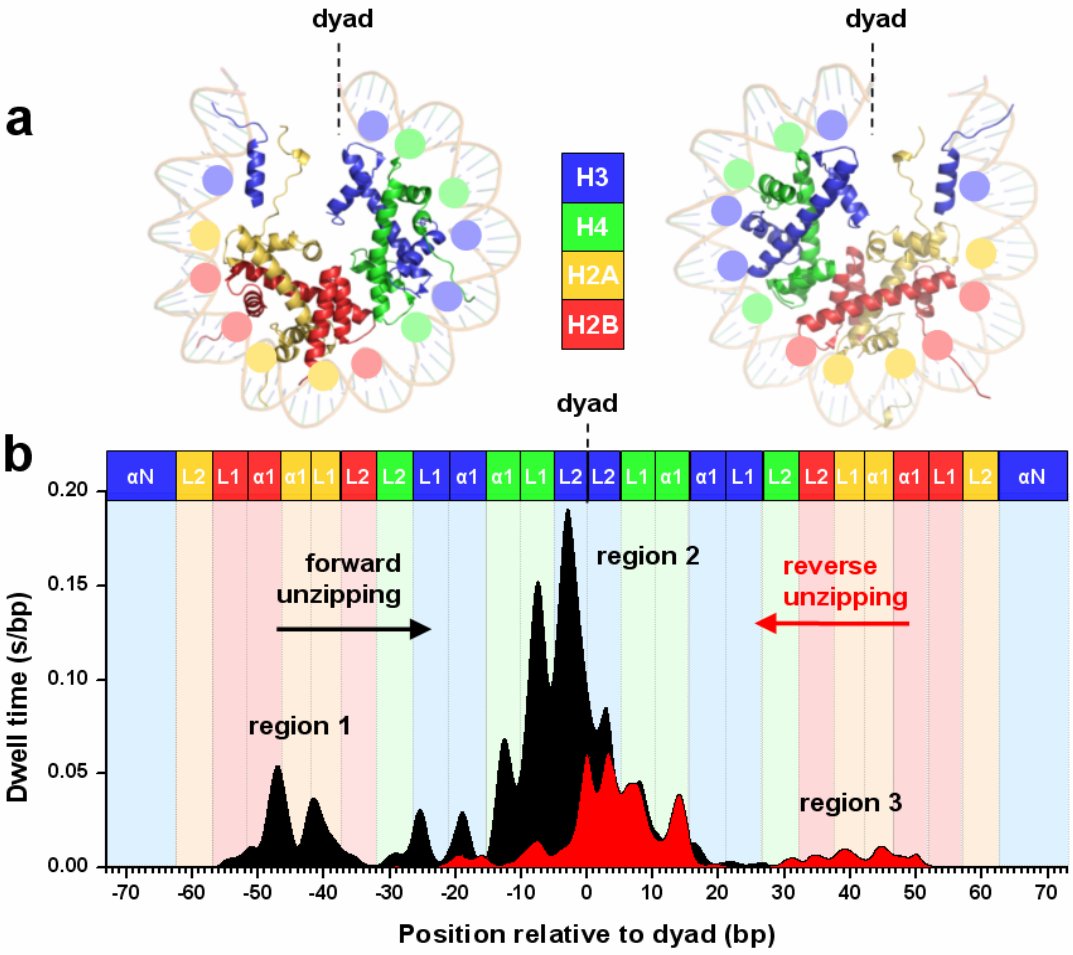
a
dyad
dyad
H3
H4
H2A
H2B
b
dyad
αN L2 L1 α1 α1 L1 L2 L2 L1 α1 α1 L1 L2 L2 L1 α1 α1 L1 L2 L2 L1 α1 α1 L1 L2 αN
forward unzipping
region 2
reverse unzipping
region 1
region 3
Dwell time (s/bp)
0.20
0.15
0.10
0.05
0.00
-70 -60 -50 -40 -30 -20 -10 0 10 20 30 40 50 60 70
Position relative to dyad (bp)

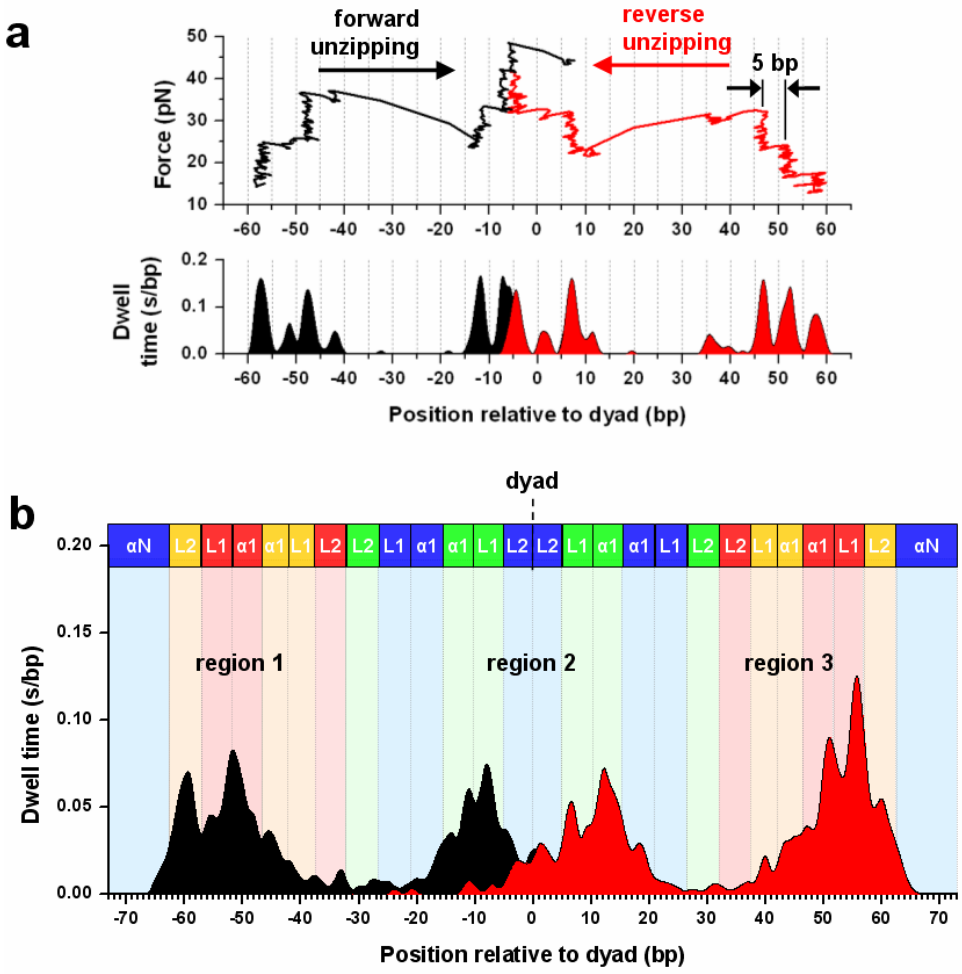


**Figure 3.6. Nucleosome disruptions under a constant loading rate. a**, Representative traces for unzipping under a constant loading rate (8 pN/s). Two traces are shown: one from forward unzipping (black) and one from reverse unzipping (red). For clarity, the naked DNA signature before and after each nucleosome disruption event is not shown. The unzipping fork again paused at specific locations, which are evident from both the traces (top) and their corresponding dwell time histograms (bottom). **b,** The average dwell time histograms of the unzipping fork under a constant loading rate. Individual traces such as those shown above were low-pass filtered to 60 Hz and their dwell time histograms were binned to 1 bp. A total of 36 traces from each direction were used for the construction. Other notations are the same as those of Figure 3.5b.

shows example traces of nucleosomes unzipped from both forward and reverse directions. Figure 3.6b shows the averaged dwell time histograms measured during both forward and reverse unzipping (for additional traces, see Figure 3.7). Aside from the aforementioned bias in the dwell time histogram, many features are consistent with data from unzipping under a constant force. The interactions near the entry and exit DNA were more evident, still showing a clear ~ 5 bp periodicity. This indicates that DNA segments at least up to 60 bp from the dyad have substantial interactions with the histone core.

***Interaction features are shared by nucleosomes on arbitrary DNA sequences***

To determine whether the conclusions above are also valid for nucleosomes of arbitrary DNA sequence or just for the 601 sequence, we assembled nucleosomes onto a DNA segment that does not contain any known positioning elements (see Methods). The assembly condition was controlled to achieve a relatively low saturation level so that each DNA molecule had at most one nucleosome. When such nucleosomal DNA molecules were unzipped with a loading rate clamp using the same conditions as those of Figure 3.6, nucleosomes were found at various locations on the template (Figure 3.8), likely due to the lack of any known nucleosome positioning element on this DNA sequence. Figure 3.8 also shows that each unzipping trace contains two (and sometime three) major regions of strong interaction, with the second region presumably located near the dyad. These nucleosomes possessed essentially identical characteristics as those of the 601 sequence, except that their peak forces within each region were typically smaller by a few pN, reflecting weaker interactions of histone with non-positioning DNA sequences. The key features remained essentially identical: the three regions of strong interactions with the strongest at the dyad, the 5 bp periodicity, and the loss of nucleosome stability upon dyad disruption. These results

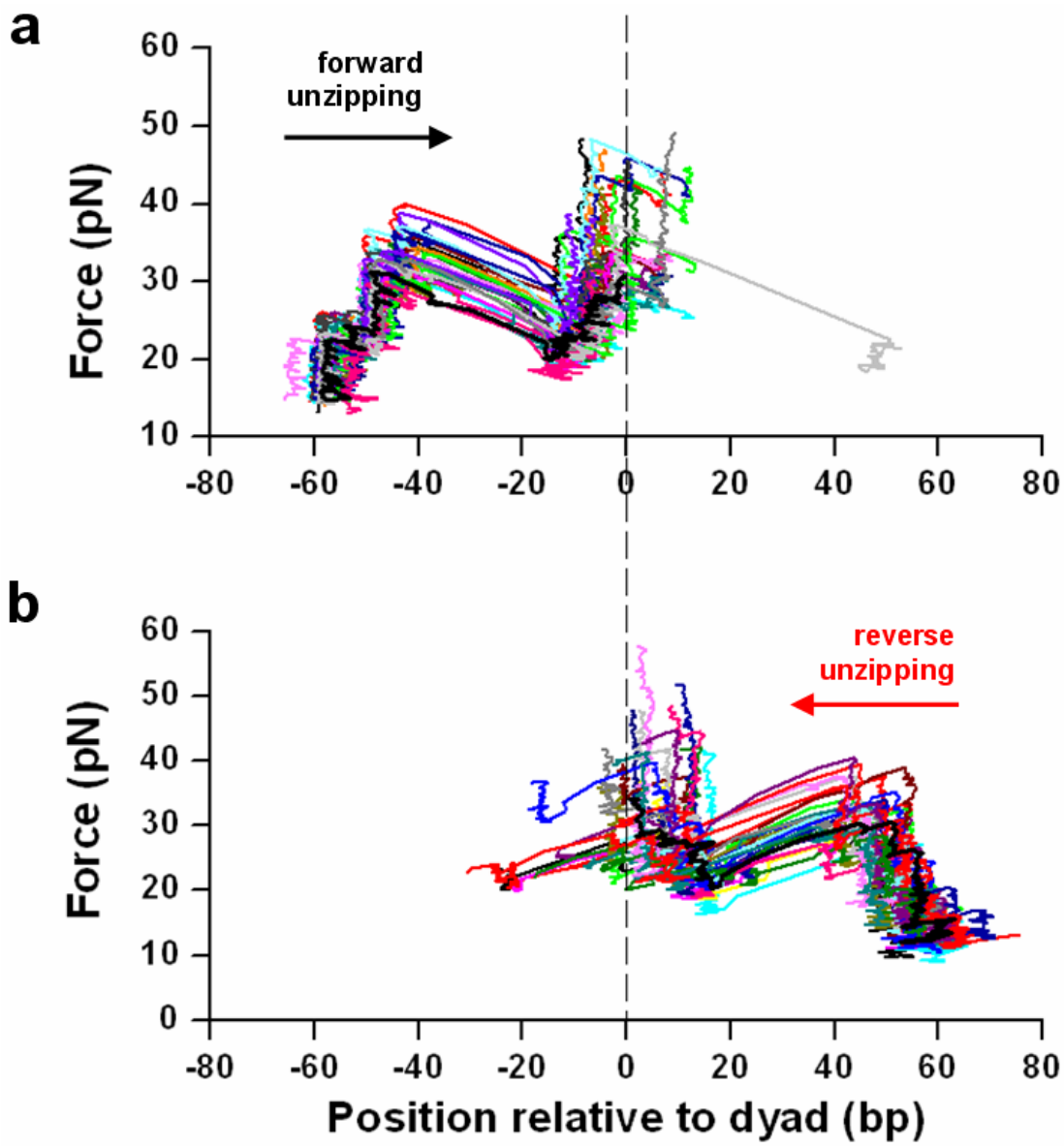


**Figure 3.7. Additional example traces of unzipping through a nucleosome under a constant loading rate.** Experimental conditions are the same as those used in Figure 3.6a. Each color represents a single trace.

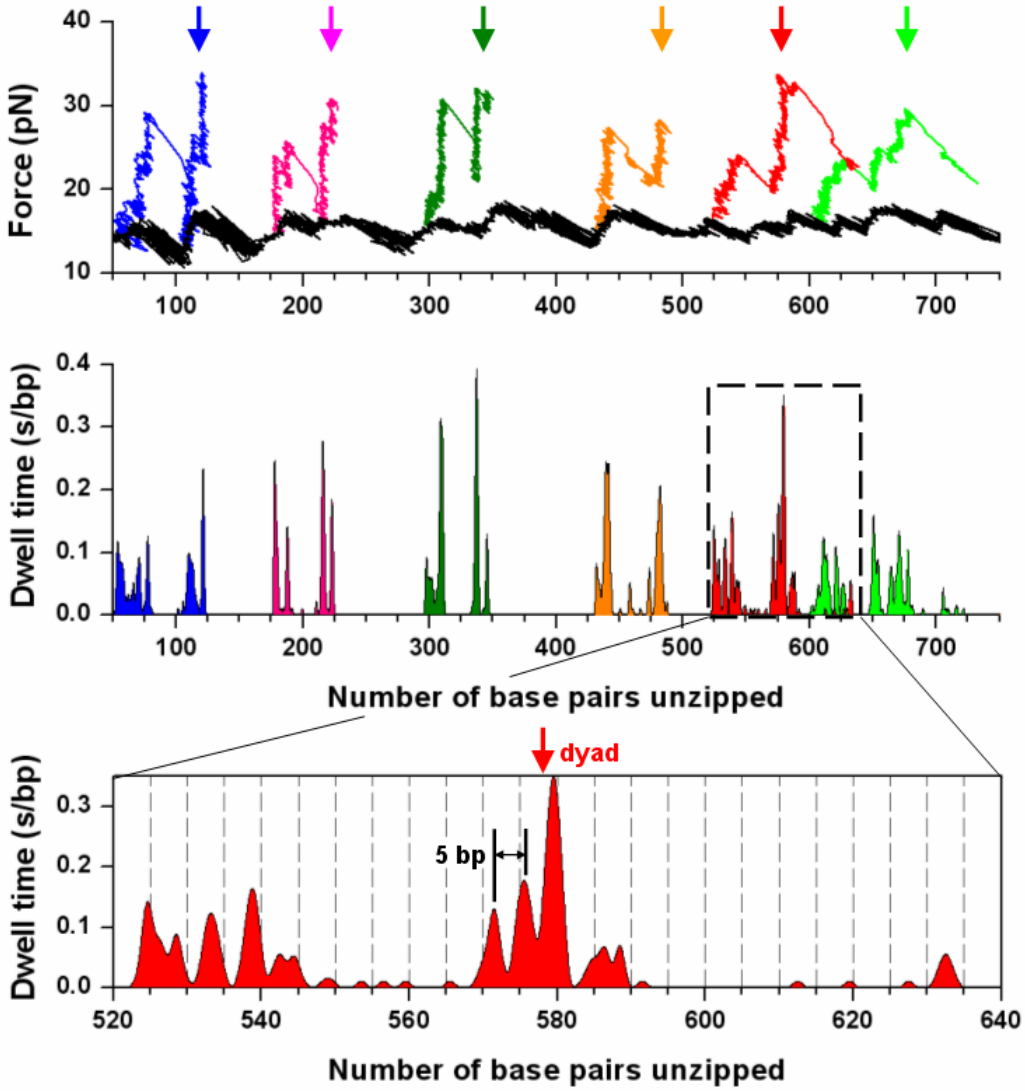


**Figure 3.8. Unzipping through a nucleosome on a DNA sequence that does not contain a positioning element.** Representative traces for unzipping under the same conditions as those of Figure 3.6. Each color was obtained from a single nucleosome unzipping event, with the unzipping force shown in the top panel and the corresponding dwell time histogram shown in the middle panel. Apparent dyad locations are indicated by vertical arrows. As a reference, an example of unzipping a naked DNA molecule of the same sequence is also shown (black). Bottom panel: Zooming in on the dwell time histogram for a specific unzipping event (red) to emphasize the periodicity.

indicate that the conclusions of this work are not restricted to nucleosomes on the 601 sequence but are general to nucleosomes on any sequence.

***Mechanical invasion of a nucleosome***

In order to mimic invasion by a motor protein as it progresses into a nucleosome, we carried out 3 sets of mechanical invasion experiments (Figure 3.9). In the first set, unzipping was allowed to proceed into and then held within the first region of strong interactions, before the DNA was relaxed to allow rezipping (Figure 3.9a). The state of the nucleosome was subsequently examined by unzipping through the entire 601 sequence. The majority of traces examined in this way (75%) showed a canonical nucleosome structure at the 601 sequence. The remaining 25% showed altered structures, likely due to incomplete re-annealing of the DNA in the presence of histones (Figure 3.10). In the second set, unzipping was allowed to proceed into and then held within the dyad region of interactions, before the DNA was relaxed to allow rezipping (Figure 3.9b). The majority of the resulting structures (70%) again resembled a canonical nucleosome at the 601 sequence. In the third set, unzipping was allowed to proceed past the dyad region of interactions, before DNA was relaxed to allow rezipping (Figure 3.9c). Subsequently, all traces showed force signatures indistinguishable from those of naked 601 sequence, indicating complete removal of the histone octamer from the 601 sequence. These results indicate that motor enzymes may be capable of accessing nearly half of the underlying DNA without resulting in histone dissociation.

***Histone-DNA interaction map of a nucleosome***

This study presents a high resolution quantitative map of histone-DNA interactions in a nucleosome. It not only provides a direct measure of locations of interactions to

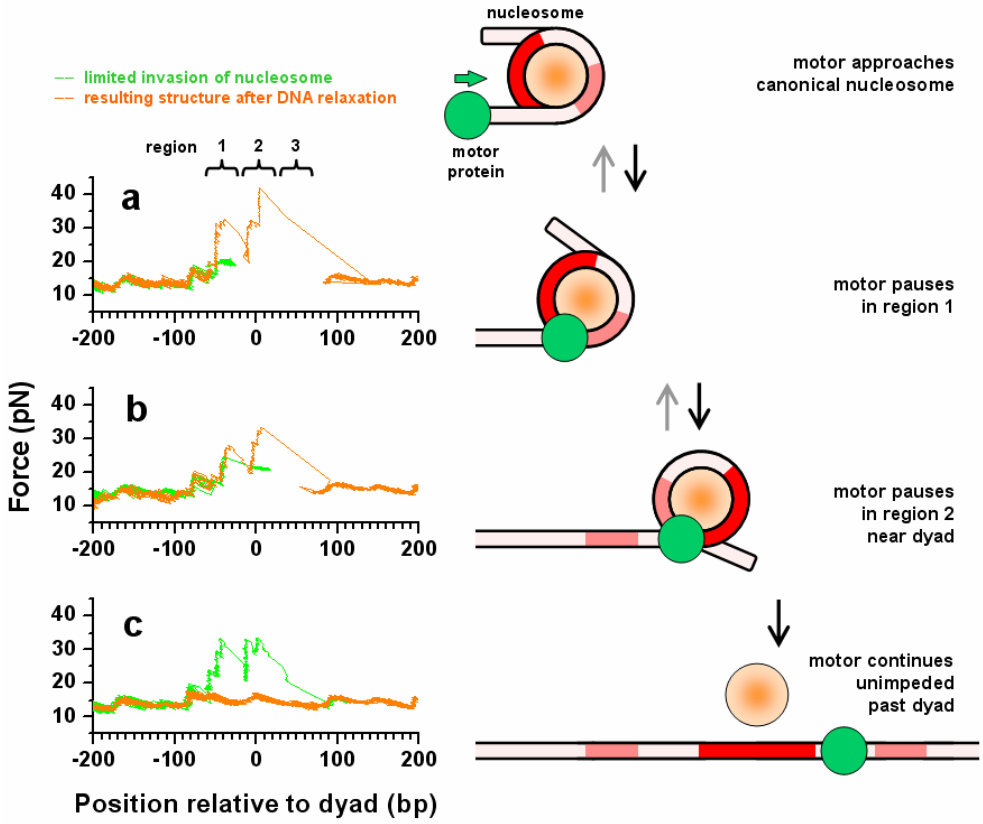


**Figure 3.9. Mechanical unzipping (left) to mimic motor enzyme progression into a nucleosome (right).** **a**, DNA was unzipped with a loading rate clamp (8 pN/s) until the unzipping force reached ~ 20 pN, which typically occurred within the 1st region of interactions (green curve). The unzipping force was then held at this force for 10 s, resulting in a horizontal force line due to the hopping of the unzipping fork among different positions within the first region. These steps mimic a motor invasion into the 1st region of interactions and subsequent pausing within the region (right). The tension in the DNA was then relaxed for ~ 3 s and the state of the nucleosome was determined by unzipping a second time (orange curve). **b**, Similar to b, except that the unzipping force was held at ~ 21 pN immediately after the unzipping fork entered the dyad region of interactions. These steps mimic motor invasion into the dyad region of interactions before pausing (right). **c**, Similar to b, except that DNA was unzipped past the dyad region of interactions. This mimics motor invasion past the dyad (right).

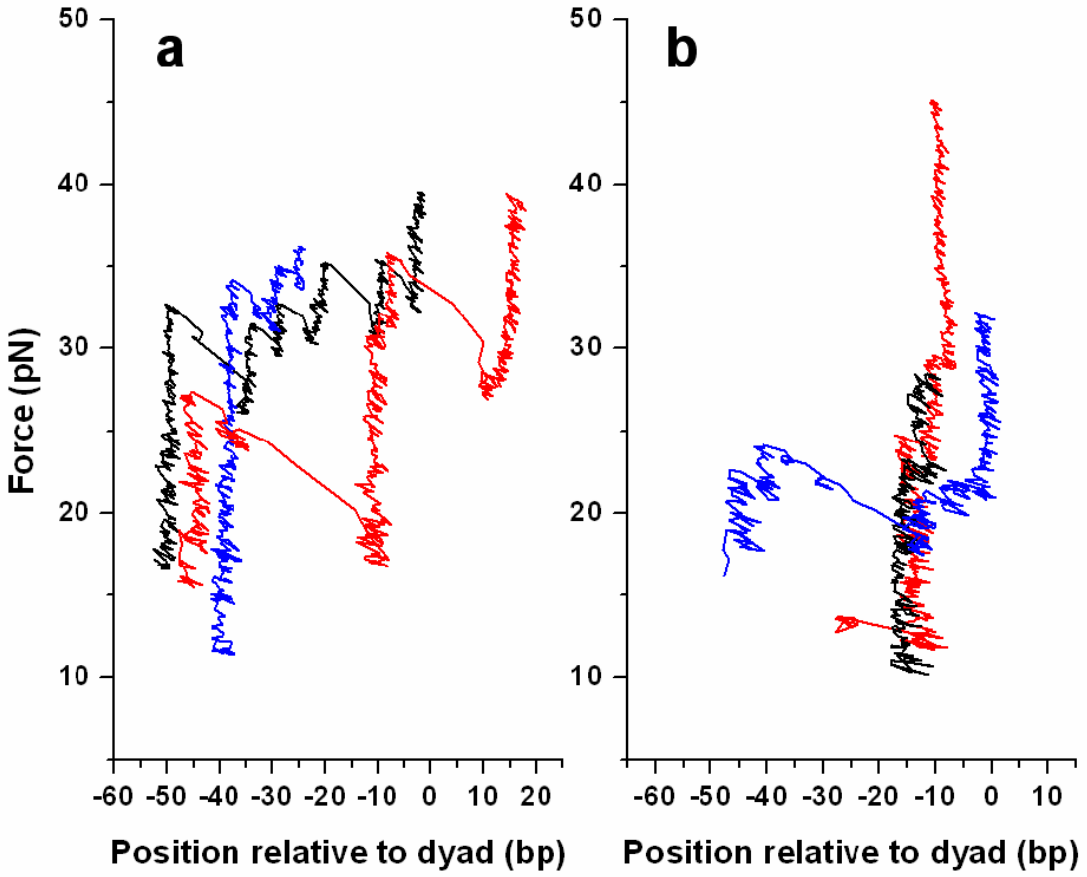


**Figure 3.10. Example traces of altered nucleosome structures after nucleosome invasion.** The mechanical invasion experiments consisted of 32 traces for the first region (Figure 3.9a), 26 traces for the second region (Figure 3.9b) and 22 traces for the entire nucleosome (Figure 3.9c). A nucleosome was considered to exhibit an altered structure if it differed from the canonical structure as defined previously [1]. For clarity, each trace is a separate color. **a,** Experimental conditions are the same as those used in Figure 3.9a. **b,** Experimental conditions are the same as those used in Figure 3.9b.

near bp, but also quantitatively assays the strengths of these interactions. The overall features of the interaction map are not specific to the 601 sequence but are shared by DNA of arbitrary sequence.

The histone-DNA interaction map reveals the existence of three regions of strong interactions. This is the most direct evidence that the histone-DNA interactions within a nucleosome are not uniform: the strongest region of interactions is located at the dyad and another two regions of strong interactions are ~ ± 40 bp from the dyad. The locations of all three regions are strongly correlated with those estimated from the crystal structure of the nucleosome [8,20]. The central region is clearly the strongest and this observation explains why nucleosome stability has been shown to be most sensitive to DNA sequence near the dyad [26]. The locations of the off-dyad regions are also consistent with findings from our previous nucleosome stretching measurements [14,17]. This also indicates that in the single molecule stretching experiments, nucleosome spool geometry may not contribute significantly to force signatures or contribute in such a way that coincides with the effects due to the two regions of off-dyad interactions. This finding is the most direct evidence for the existence of the three regions and should resolve the ongoing controversy on this issue.

A 5 bp periodicity in the interaction map was observed whereas prior to this work a 10 bp periodicity would have been expected. The crystal structure of the nucleosome shows that specific DNA-histone contacts are made each time the DNA minor groove faces the histone octamer surface, leading to binding sites spaced at ~10 bp (the helical pitch of dsDNA) [1]. Closer inspection shows that interactions from the two strands of the dsDNA completely stagger with each other and alternate between the two strands along the sequence at every 5 bp. However, in crystal structure analyses histone

interaction with each minor groove of the DNA has been treated as a single binding site [1,20,27]. This is reasonable since disruption of a histone interaction with one of the DNA strands at a minor groove may result in a concurrent disruption of a histone interaction with the other strand. Prior to our experiments, we had anticipated observation of a 10 bp periodicity. The fact that we have actually observed a 5 bp periodicity indicates that the histone interactions with two strands of DNA at its minor groove are rather decoupled, and can thus be disrupted sequentially instead of simultaneously.

The interactions near exit and entrance DNA were found to be particularly weak, although they maintain the 5 bp periodicity. These weak interactions are expected to permit spontaneous peeling of DNA ends from the octamer surface as observed by equilibrium accessibility assays [28,29].

***Implication for transcription***

The histone-DNA interaction map has significant implications for how RNA polymerases may gain access to DNA associated with a nucleosome. Although RNA polymerases are known to be powerful molecular motors [30,31], the presence of a nucleosome still presents a major obstacle [2-7]. The mechanical unzipping experiments described here resemble the action of RNA polymerase which opens up a transcription bubble and unzips the downstream DNA while advancing into a nucleosome (right panel of Figure 3.9). These experiments require both flexibility and precision control in positioning the unzipping fork to specific locations inside a nucleosome, something that is not currently possible to achieve in biochemical experiments. The histone-DNA interaction map (Figure 3.5) makes a number of experimentally verifiable predictions. When the RNA polymerase begins to invade the nucleosomal DNA, it is

expected to initially proceed rather smoothly, but pause when it encounters the off-dyad interactions. Disruption of these interactions permits it to proceed toward the dyad. The polymerase will then pause most strongly within the dyad region of interactions. Once it overcomes the dyad interactions, it will proceed through the rest of the nucleosomal DNA with minimal resistance. The interaction map also predicts that the 601-positioned nucleosome acts as a polar barrier to transcription: transcription in the forward direction is less efficient than in the reverse direction. Interestingly, all of these predictions have been verified by biochemical studies of Pol II or Pol III transcription through nucleosomes [2-7]. While the interaction map also suggests that transcription pausing may exhibit a finer ~ 5 bp periodic pattern, an ~ 10 bp periodicity has been observed [5,6,32,33]. Although this periodicity has been attributed to nucleosome restriction of RNAP rotation coupled with DNA loop formation, this work offers a simpler explanation. The ~ 10 bp periodicity in transcription pausing may be due to RNA polymerase cooperatively disrupting a pair of interactions located at each minor groove of DNA.

Although the pausing pattern of RNA polymerase is dictated by both the mechanical barriers encountered as well as its own motor properties, similarities between the dwell time in the histone-DNA interaction map (Figure 3.5b) and the polymerase pausing pattern within a nucleosome suggest that the barriers encountered by the polymerase are a major determinant of its pausing behavior. Thus, this explanation of the pausing pattern within a nucleosome based on the histone-DNA interaction map provides a simpler explanation than existing models [3,5,32]. The consistency of the histone-DNA interaction map with biochemical assays of RNA polymerase pausing pattern is an indication that this map may also be used to predict how other motor enzymes pass through nucleosomes.

The results from nucleosome invasion experiments yield testable predictions regarding the fate of nucleosomes during transcription. If RNA polymerase backtracks before the dyad, histones will not dissociate from the DNA but will tend to reform a canonical nucleosome at the same location, perhaps encouraging further backtracking of the polymerase. Once the RNA polymerase passes the dyad, histones will most likely be removed from their original locations.

***Histone-histone interactions***

Although the nucleosome invasion experiments did not directly detect histone-histone interactions, those results do provide some indication for H2A/H2B dimer interaction with the H3/H4 tetramer. Figure 3.9b shows that unzipping up to the dyad allowed recovery of a canonical nucleosome upon relaxation of the DNA. This indicates that the dimer did not dissociate after losing protection from half of the nucleosomal DNA. Note that there were no added free histones in the buffer (i.e. infinite dilution of histones), so any loss of histones from the DNA would have been effectively irreversible. Our observation thus indicates that the H2A/H2B dimer can remain stably bound to the H3/H4 tetramer for at least 10 seconds (the duration of the experiment) when DNA unravels from the surface of the histone core. This also implies that if a motor protein can proceed through a nucleosome at a reasonable rate, the histone octamer may remain intact until its dissociation from the DNA.

Our experimental approach has the sensitivity to detect asymmetry in histone-DNA interactions across a nucleosome on a positioning sequence. Likely, asymmetries of this sort exist in eukaryotic genomes, and may have functional importance for normal

gene expression where positioned nucleosomes reside at key positions transited by Pol II [34].

***Methods***

Nucleosomal DNA templates were prepared using methods similar to those previously described [16]. Briefly, each DNA construct consisted of two separate segments (Figure 3.1a). An ~1.1 kbp anchoring segment was prepared by PCR from plasmid pRL574 [35] using a digoxigenin-labeled primer and then digested with *Bst*XI (NEB) to produce a ligatable overhang. Each unzipping segment was prepared by PCR using a biotin-labeled primer and then digested with *Bst*XI and dephosphorylated using CIP (NEB) to introduce a nick into the final DNA template. Nucleosomes were assembled from purified HeLa histones onto the unzipping fragment by a well established salt dialysis method [36]. The two segments were joined by ligation immediately prior to use. This produced the complete template that was labeled with a single dig tag on one end and a biotin tag located 7 bp after the nick in one DNA strand.

The forward 601 unzipping segment is ~ 0.8 kbp and was prepared by PCR from plasmid 601 [24] as described previously [16]. The reverse template is nearly identical to the forward template, except that the reverse unzipping segment was flipped so that the unzipping fork would approach the nucleosome from the opposite direction. To achieve this, the reverse segment was produced via different primers, such that the ligatable overhang produced through *Bst*XI digestion and nick introduced via CIP were located on the end opposite that of the forward segment. The unzipping segment that does not contain any known nucleosome positioning element is ~ 0.8 kbp and was prepared by PCR from plasmid pBR322 (NEB).

Three different hairpin templates were prepared from the forward template (without nucleosomes) by truncating the unzipping segment at precise locations via restriction enzymes and ligating the same hairpin onto the end in each case. The lengths of the unzipping templates are indicated in Figure 3.2b.

For experiments involving unzipping through a nucleosome under a constant force, the unzipping started with a loading rate clamp (8 pN/s) until the desired force of ~28 pN was reached within a nucleosome. The unzipping force was then held constant via feedback control of the coverslip position [25]. This force is much higher than the sequence-dependent unzipping force of the naked 601 sequence (13-16 pN), minimizing the dwell time contribution due solely to DNA base pairing interactions, but is small enough to allow sufficient dwell time at each DNA sequence position for detection. Upon reaching the end of the 601 sequence, the unzipping was continued under a loading rate clamp (8 pN/s). Unzipping before and after the 601 segment under a constant loading rate generated distinct unzipping signatures that could be used for data alignment (see below).

An optical trapping setup was used to unzip a single DNA molecule by moving the microscope coverslip horizontally away from the optical trap (Supplementary Fig 1b). As barriers to fork progression were encountered, a computer-controlled feedback loop increased the applied load linearly with time (8 pN/s) as necessary to overcome those barriers. Whenever the unzipping fork stopped, e.g., at an interaction, the unzipping force was ramped up linearly with time until the interaction was disrupted [37]. When two interactions occurred in close vicinity, upon the disruption of the first interaction the force was unable to relax back to the baseline before being ramped up again for the second interaction, subjecting this subsequent interaction to a higher

initial force. Therefore, for each region of interactions, the dwell time histogram highlighted the edge of the region first encountered. Another feature of this method was the display of the distinctive force signature for a nucleosome, allowing for ease of identification of the nucleosome structure [16] (compare traces in Figure 3.4 with Figure 3.7).

Data were low pass filtered to 5 kHz, digitized at ~12 kHz and later filtered to 60 Hz. Previously, to improve the positional precision and accuracy, the experimental curves were aligned to the theoretical curve by cross-correlation of a region immediately preceding the nucleosome disruption [16]. In the current work, the precision and accuracy were further improved by an additional cross-correlation of a region immediately following the nucleosome disruption. To account for minor instrumental drift, trapping bead size variations, and DNA linker variations, the alignment allowed for a small additive shift (< 5 bp) and multiplicative linear stretch (< 2%) using algorithms similar to those previously described [38].

**Acknowledgements** We thank members of the Wang lab and Dr. B. Brower-Toland for critical reading of the manuscript, J. Jin for helpful advice with biochemical preparations, and Dr. D.S. Johnson for helpful discussions on instrumentation. We wish to acknowledge support from NIH grants (GM059849 to M.D.W; GM25232 to J.T.L.), the Keck Foundation (to M.D.W), the Cornell Nanobiotechnology Center (to M.D.W. and J.T.L.), and the Molecular Biophysics Training Grant Traineeship (to M.A.H.).

REFERENCES


1. Luger, K., Mader, A.W., Richmond, R.K., Sargent, D.F. & Richmond, T.J. Crystal structure of the nucleosome core particle at 2.8 A resolution. *Nature* **389**, 251-60 (1997).
2. Bondarenko, V.A. et al. Nucleosomes can form a polar barrier to transcript elongation by RNA polymerase II. *Mol Cell* **24**, 469-79 (2006).
3. Kireeva, M.L. et al. Nature of the nucleosomal barrier to RNA polymerase II. *Mol Cell* **18**, 97-108 (2005).
4. Kireeva, M.L. et al. Nucleosome remodeling induced by RNA polymerase II: loss of the H2A/H2B dimer during transcription. *Mol Cell* **9**, 541-52 (2002).
5. Studitsky, V.M., Kassavetis, G.A., Geiduschek, E.P. & Felsenfeld, G. Mechanism of transcription through the nucleosome by eukaryotic RNA polymerase. *Science* **278**, 1960-3 (1997).
6. Studitsky, V.M., Walter, W., Kireeva, M., Kashlev, M. & Felsenfeld, G. Chromatin remodeling by RNA polymerases. *Trends Biochem Sci* **29**, 127-35 (2004).
7. Walter, W., Kireeva, M.L., Studitsky, V.M. & Kashlev, M. Bacterial polymerase and yeast polymerase II use similar mechanisms for transcription through nucleosomes. *J Biol Chem* **278**, 36148-56 (2003).
8. Davey, C.A., Sargent, D.F., Luger, K., Maeder, A.W. & Richmond, T.J. Solvent mediated interactions in the structure of the nucleosome core particle at 1.9 Å resolution. *J Mol Biol* **319**, 1097-113 (2002).
9. Cosgrove, M.S., Boeke, J.D. & Wolberger, C. Regulated nucleosome mobility and the histone code. *Nat Struct Mol Biol* **11**, 1037-43 (2004).
10. Kouzarides, T. Chromatin modifications and their function. *Cell* **128**, 693-705 (2007).

11. Segal, E. et al. A genomic code for nucleosome positioning. *Nature* **442**, 772-8 (2006).
12. Bancaud, A. et al. Nucleosome chiral transition under positive torsional stress in single chromatin fibers. *Mol Cell* **27**, 135-47 (2007).
13. Bennink, M.L. et al. Unfolding individual nucleosomes by stretching single chromatin fibers with optical tweezers. *Nat Struct Biol* **8**, 606-10 (2001).
14. Brower-Toland, B.D. et al. Mechanical disruption of individual nucleosomes reveals a reversible multistage release of DNA. *Proc Natl Acad Sci U S A* **99**, 1960-5 (2002).
15. Cui, Y. & Bustamante, C. Pulling a single chromatin fiber reveals the forces that maintain its higher-order structure. *Proc Natl Acad Sci U S A* **97**, 127-32 (2000).
16. Shundrovsky, A., Smith, C.L., Lis, J.T., Peterson, C.L. & Wang, M.D. Probing SWI/SNF remodeling of the nucleosome by unzipping single DNA molecules. *Nat Struct Mol Biol* **13**, 549-54 (2006).
17. Brower-Toland, B. et al. Specific contributions of histone tails and their acetylation to the mechanical stability of nucleosomes. *J Mol Biol* **346**, 135-46 (2005).
18. Gemmen, G.J. et al. Forced unraveling of nucleosomes assembled on heterogeneous DNA using core histones, NAP-1, and ACF. *J Mol Biol* **351**, 89-99 (2005).
19. Pope, L.H. et al. Single chromatin fiber stretching reveals physically distinct populations of disassembly events. *Biophys J* **88**, 3572-83 (2005).
20. Luger, K. & Richmond, T.J. DNA binding within the nucleosome core. *Curr Opin Struct Biol* **8**, 33-40 (1998).

21. Mihardja, S., Spakowitz, A.J., Zhang, Y. & Bustamante, C. Effect of force on mononucleosomal dynamics. *Proc Natl Acad Sci U S A* **103**, 15871-6 (2006).

22. Kulic, I.M. & Schiessel, H. DNA spools under tension. *Phys Rev Lett* **92**, 228101 (2004).

23. Sakaue, T. & Lowen, H. Unwrapping of DNA-protein complexes under external stretching. *Phys Rev E Stat Nonlin Soft Matter Phys* **70**, 021801 (2004).

24. Lowary, P.T. & Widom, J. New DNA sequence rules for high affinity binding to histone octamer and sequence-directed nucleosome positioning. *J Mol Biol* **276**, 19-42 (1998).

25. Johnson, D.S., Bai, L., Smith, B.Y., Patel, S.S. & Wang, M.D. Single-molecule studies reveal dynamics of DNA unwinding by the ring-shaped T7 helicase. *Cell* **129**, 1299-309 (2007).

26. Thastrom, A., Bingham, L.M. & Widom, J. Nucleosomal locations of dominant DNA sequence motifs for histone-DNA interactions and nucleosome positioning. *J Mol Biol* **338**, 695-709 (2004).

27. Muthurajan, U.M. et al. Crystal structures of histone Sin mutant nucleosomes reveal altered protein-DNA interactions. *EMBO J* **23**, 260-71 (2004).

28. Li, G., Levitus, M., Bustamante, C. & Widom, J. Rapid spontaneous accessibility of nucleosomal DNA. *Nat Struct Mol Biol* **12**, 46-53 (2005).

29. Li, G. & Widom, J. Nucleosomes facilitate their own invasion. *Nat Struct Mol Biol* **11**, 763-9 (2004).

30. Wang, M.D. et al. Force and velocity measured for single molecules of RNA polymerase. *Science* **282**, 902-7 (1998).

31. Galburt, E.A. et al. Backtracking determines the force sensitivity of RNAP II in a factor-dependent manner. *Nature* **446**, 820-3 (2007).

32. Studitsky, V.M., Clark, D.J. & Felsenfeld, G. Overcoming a nucleosomal barrier to transcription. *Cell* **83**, 19-27 (1995).

33. Bednar, J., Studitsky, V.M., Grigoryev, S.A., Felsenfeld, G. & Woodcock, C.L. The nature of the nucleosomal barrier to transcription: direct observation of paused intermediates by electron cryomicroscopy. *Mol Cell* **4**, 377-86 (1999).

34. Albert, I. et al. Translational and rotational settings of H2A.Z nucleosomes across the Saccharomyces cerevisiae genome. *Nature* **446**, 572-6 (2007).

35. Schafer, D.A., Gelles, J., Sheetz, M.P. & Landick, R. Transcription by single molecules of RNA polymerase observed by light microscopy. *Nature* **352**, 444-8 (1991).

36. Lee, K.M. & Narlikar, G. Assembly of nucleosomal templates by salt dialysis. *Curr Protoc Mol Biol* **Chapter 21**, Unit 21 6 (2001).

37. Koch, S.J., Shundrovsky, A., Jantzen, B.C. & Wang, M.D. Probing protein-DNA interactions by unzipping a single DNA double helix. *Biophys J* **83**, 1098-105 (2002).

38. Deufel, C. & Wang, M.D. Detection of forces and displacements along the axial direction in an optical trap. *Biophys J* **90**, 657-67 (2006).

# Chapter 4:
# The T-structure:
# unzipping double stranded DNA under tension

***Motivation for a new assay***

Optical trapping configurations may be sorted into three categories: (1) measuring force and extension during a dsDNA stretch (Figure 4.1a); (2) measuring force and extension (i.e. number of base pairs unzipped) during mechanical strand separation (Figure 4.1b); (3) measuring force, extension, torque and linking number simultaneously by using linearly polarized beam to control the angular rotation of a birefringent quartz cylinder (Figure 4.1c). The configuration chosen depends upon the requirements of a particular experiment.

The simultaneous stretching and twisting of dsDNA is achieved by axially stretching torsionally constrained DNA in an angular optical trap[1,2]. However, the unzipping method, as described in Chapters 2 and 3, has been incompatible with both stretching and twisting experiments. This is unfortunate because the mechanical separation of dsDNA provides a powerful basis for the high precision detection of protein-DNA interaction sites. The precision and accuracy of this technique have nearly reached their practical limit of ~ 1 bp and have easily surpassed it in terms of resolution. Combining the unzipping and stretching techniques would open up new types of experiments; for example, obtaining the histone-DNA interaction map for partially unwrapped nucleosomes under tension or determining the structure of overstretched dsDNA. Combining the unzipping and twisting techniques would bring the power of the unzipping technique to bear on other exotic DNA structures, such as overwound P-DNA[3] and melted, underwound L-DNA[4] or allow one to study the mechanical separation of twisted DNA.

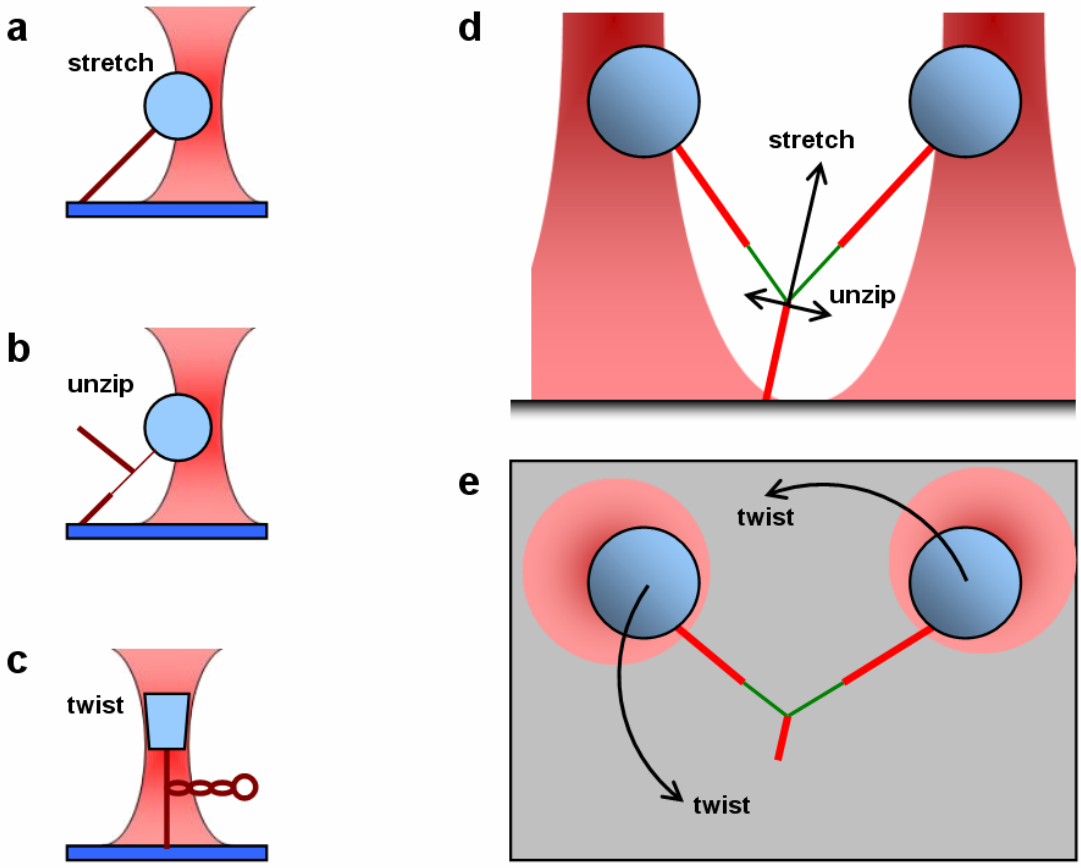


**Figure 4.1. The T-structure permits combination of all existing single molecule trapping assays.** (a-c) Almost all single molecule experiments are represented by either (a) stretching, (b) unzipping or (c) twisting experiments. Twisting and stretching experiments are easily combined by stretching along the axial direction. (d) The T-structure assay combines stretching and unzipping for the first time by attaching the unzipping segment to the surface of a coverslip. Unzipping can be controlled by increasing the distance between the optical traps whereas the tension along the unzipping segment can be controlled by adjusting the XYZ position of the piezo stage. (e) Twisting could be incorporated by rotating each of the beads around the trunk attachment point. In our instrument, this would be accomplished in practice through the coordination of moving the steered trap and the XYZ piezo around the fixed trap.

***The T-structure: template design***

We decided to design a DNA construct that could, in principle, be used to combine all three types of experiments simultaneously. To achieve this, we generated a construct comprising three pieces of dsDNA that come together at a 3-way junction. Two arms of DNA may be manipulated independently via two separate polystyrene beads using our dual bead optical trapping apparatus (Figure 2.4), whereas the far end of the third, unzipping segment has been designed to attach to the surface of a cover slip so that it may be manipulated independently via an XYZ piezo stage. We refer to the completed construct as the "T-structure" and an illustration is shown in Figure 4.1d. The completed T-structure is a versatile construct. The distance between the fixed and steered trap control the horizontal force component along the T-trunk, which encourages strand separation (Figure 4.1d); the Z position of the XYZ piezo stage controls the vertical force along the T-trunk, which stretches the dsDNA unzipping segment (Figure 4.1d); the linking number of the unzipping segment could be changed by moving the steered beam and the XYZ stage in a coordinated fashion in the XY plane (Figure 4.1e).

Attachment to both the surface and two different beads requires three distinct bonds with both high affinity and high specificity. The unzipping segment ("trunk" or "T-trunk") was produced via PCR from the pLB601 plasmid where one of the primers was labeled with a fluorescein on a thymine base one base from the end. Two unzipping arms were made via PCR ("T-arm1" and "T-arm2") from plasmids pRL574 and pBR322 using primers labeled with digoxigenin and biotin, respectively. These three pieces were attached via a 3-way dsDNA junction via 4 oligonucleotides ("upper 1/2", "lower 1/2") that were heated above their melting temperature and carefully annealed by setting them at room temperature to allow them to cool slowly. The

annealed products ("upper 1" + "lower 1" and "upper 2" + "lower 2") were ligated to their respective arms via distinct restriction enzyme overhangs (BstXI and BstEII, respectively), were purified via Agarose gel extraction and then the resulting arms were heated and reannealed together before finally ligating that product to the purified trunk with the appropriate restriction enzyme overhang (AlwNI). A detailed protocol is reproduced below and illustrated in Figure 4.2, for clarity:

1. PCR each of the Arms and spin purify.
    a. T-Arm1 (1835 bp)

       Plasmid: pRL574

       Primer1: P17-F-dig-pRL574 (Dig-CTATGCGGCATCAGAGCAGATTG)

       Primer2: T-Arm1-R-BstXI (GATCCAGATCGTTGGTGAAC)
    b. T-Arm2 (2013 bp)

       Plasmid: pBR322

       Primer1: P2-F-biotin-pBR322 (Bio-GATGCTTTTCTGTGACTGGTGAG)

       Primer2: T-Arm2-R-BstEII (ACGGTTACCAGCCTAGCCGGGTCCTCA)
2. PCR the T-Trunk and spin purify.
    a. T-Trunk (3848 bp)

       Plasmid: pLB601

       Primer1: T-Trunk-F-Fl (C(FluorT)TGAGCGTCGATTTTTGTGAT)

       Primer2: T-trunk-R-AlwNI (CGCAGCTACTGGCGAAAGGGGGATGT)
3. Digest the results with their corresponding enzymes and spin purify.

a. T-Arm1 – BstXI
b. T-Arm2 – BstEII
c. T-Trunk – AlwNI

4. Anneal upper1 with lower1 and upper2 with upper2:
   a. 2 uL upper1 + 2 uL lower1 + 16 uL H2O

      upper1: /phos/GCAGTACCGAGCTCATCCAATTCTACATGCCGC

      lower1:

      /phos/GCCTTGCACGTGATTACGAGATATCGATGATTGCGGCG

      GCATGTAGAATTGGATGAGCTCGGTACTGCATCG
   b. 2 uL upper2 + 2 uL lower2 + 16 uL H2O

      upper2: CGTTACGTCATTCTATACACTGTACAG

      lower2:

      /phos/GTAACCTGTACAGTGTATAGAATGACGTAACGCGCAAT

      CATCGATATCTCGTAATCACGTGCAAGGCCTA
   c. Use “ANNL28” program on old PCR machine.
5. Ligate each T-Arm with its corresponding upper-lower annealed product:
   a. Upper-lower : T-Arm = 10:1
   b. Ligate at RT for 2+ hours.
6. Gel purify each T-Arm ligation to remove excess annealed-products, which cannot be removed via normal spin purifications.
7. Anneal the two T-Arm products together.
   a. T-Arm1 : T-Arm2 = 1:1
   b. Incubate at 55C for 20+ mins and then set at RT for 10+ mins.
8. Ligate T-Trunk from step 3 to the annealed T-Arms from step 7.
   a. T-Trunk : T-Arms = 4:1
   b. Ligate at 16C for at least 30 minutes.

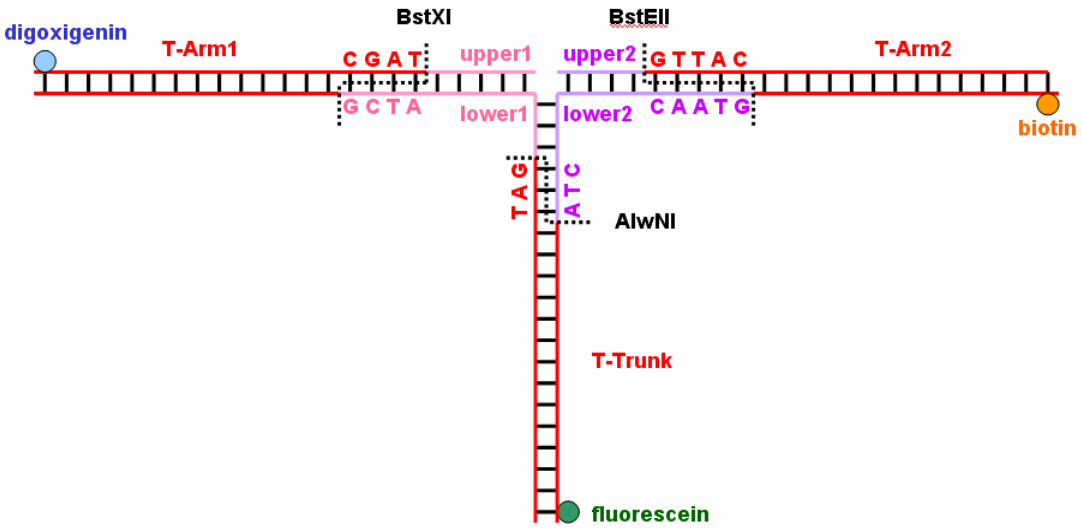


**Figure 4.2. The T-structure DNA construct.** As described in the main text, both arms and the trunk are produced via PCR from different plasmids. Each segment contains a unique attachment label (digoxigenin, biotin or fluorescein) that binds with high affinity to a conjugate pair (anti-digoxigenin, streptavidein or anti-fluorescein) ensuring that each segment is capable of being manipulated separately. The design is modular so that a variety of trunks may be attached, so long as they contain an AlwNI restriction enzyme overhang on one end.

***Calibration of a dual beam optical trap***

Force detection along the X and Y dimensions is accomplished by analyzing the deflection of each beam separately using two position sensitive detectors (PSD) – in our case, quadrant photo diodes (Figure 2.4). As described in Chapter 2, since light has a momentum, beam deflections detected at the PSD are measurements of the force applied to polystyrene beads trapped in the sample plane. The calibration procedure for X and Y detection are well established and I have followed procedures that are very similar to those described previously[5]. Briefly, prior to a trapping experiment, the quadrant photodiodes are adjusted so that the undeflected beams provide equal intensity to each of the four quadrants. For a deflected beam, some of the quadrants record higher intensity than the others and a weighted average over the four quadrants provides a spatial measurement of beam position. This measurement of beam deflection may be thought of as either (a) a direct measurement of force in units of volts or, because the force is proportional to the first derivative of its Gaussian intensity profile within a few hundred nanometers on either side of the trap center, (b) a measurement of bead displacement in volts. The proportionality constant between volts and piconewtons may be determined using various methods and, for our instrument, is generally determined by finding the corner frequency of a free bead at the trap center as a function of laser power[5].

Force detection along the Z axis is fundamentally different than in X and Y. Instead of measuring bead deflection, the position of a trapped polystyrene bead along Z utilizes interferometry at the detection plane which depends on the Gouy phase anomaly of a focused beam. Forward scattered light from the trapped polystyrene beads interferes with unscattered light and results in a light intensity that varies with the position of the particle along the axial dimension of an optical trap. The sum of

the intensity on all four quadrants of the PSD for each beam served as a raw signal for Z detection and these were both normalized by the input laser power measured immediately after recombination of beams after the tip/tilt mirror to reduce noise resulting from changes in the laser power that were not the result of axial displacements of the beads[6].

The existence of a second, steered beam required one additional calibration for the case of Z measurements. As shown in Figure 4.3, the raw X and Z signals varied as the steered beam was steered via changes in the tip/tilt mirror. Changes in the X signal were only observed in the case of the steered trap (Figure 4.3, top right), which probably arises due to imperfections in mapping the plane of the tip/tilt mirror to the back focal plane. Such imperfections suggest that rotations of the beam at the tip/tilt mirror will not manifest themselves purely as translations in the sample plane, causing an apparent beam deflection for the steered beam at the detection plane of the PSD. Since changes in the X signal were observed to be nearly linear, this was accounted for by applying a linear correction to the raw X signals for the steered trap. Changes in the Z signal were more complicated and could not be simply accounted for via a linear adjustment. Therefore, a lookup table was generated for the Z signal observed for both the fixed and the steered trap as a function of steered trap position (Figure 4.3, bottom left and bottom right, respectively). The Z offset signal exhibited similar behavior for both traps. After an experiment, Z signals were corrected by subtracting an offset interpolated from the table based on the actual XY position of the steered trap.

T-structure unzipping occurs in the XZ plane. As tension applied along the trunk increases, the bead will be pulled further away from the trap center along the Z axis.

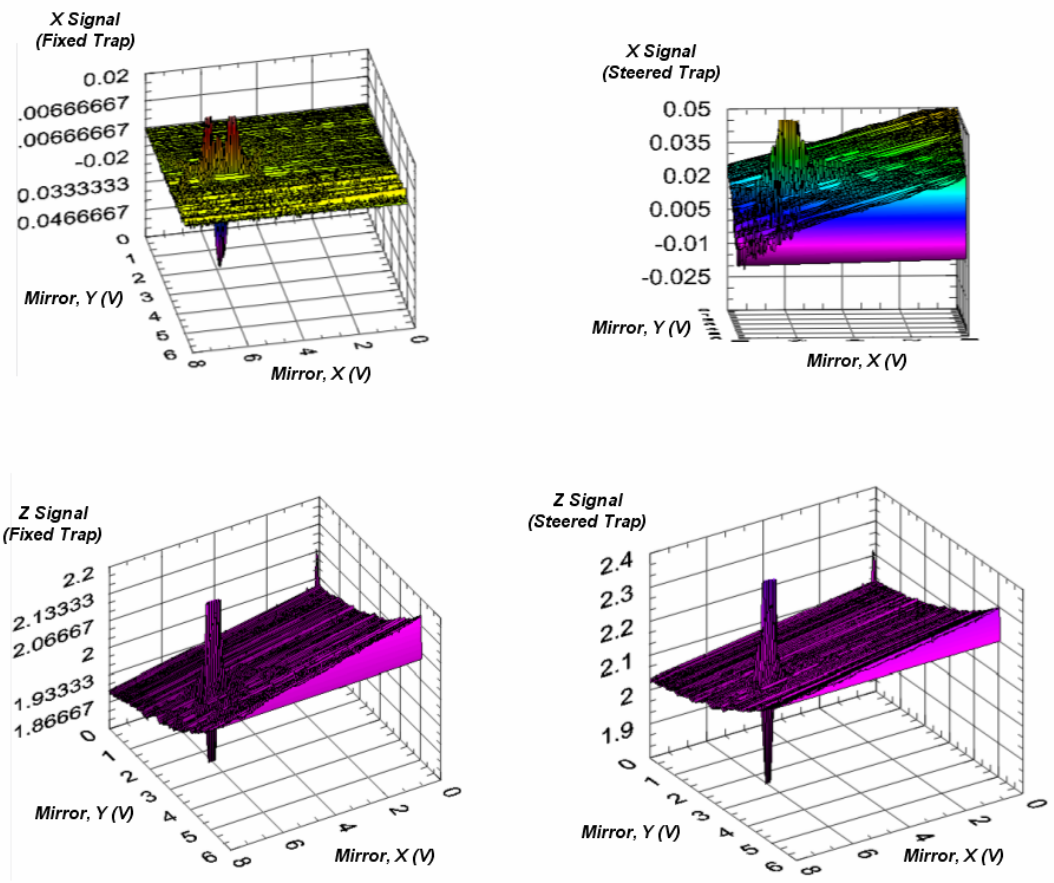


**Figure 4.3. Generation of X and Z signal offset lookup tables.** (top, left and right) Imperfections in mapping the reflection plane of the tip/tilt mirror to the back focal plane of the objective result in offsets to the X signals observed by the PSD for the steered beam. Since this does not affect the fixed beam, no offset is necessary over the full range of tip/tilt motion. (bottom, left and right) Offsets in the Z signal are observed for both traps and they follow similar behavior. We attribute this effect to minor clipping of the outer edge of the beam at the input power detector, which is used to normalize the Z signal.

Analogously, as the X component of the force along the arms increases, the beads will be pulled out of the trap along the X axis. The trap stiffness is highest at the beam waist and changes as beads are displaced from it. Therefore, the trap stiffness had to be calibrated over the full XZ plane and is accounted for both during the data acquisition process as well as during final data conversion.

***Data collection: unzipping the T-structure***

Sample chambers using the T-structure are performed similarly as for the single beam chamber, described in detail below:

1. A chamber (~ 15-20 uL volume) is constructed by attaching long, narrow strips of double stranded tape between a microscope slide and a cover slip.
2. Incubate chamber for ~ 5 minutes with ~ 20 uL of anti-fluorescein diluted in sample buffer.
3. Flow in ~ 35 uL of casein (4 mg / mL) and incubate for ~ 5 minutes.
4. Wash chamber with ~ 50 uL of sample buffer.
5. Flow in ~ 20 uL of the completed T-structure DNA (annealed arms at 250 pM) and incubate for ~ 10 minutes.
6. Wash chamber with ~ 50 uL of sample buffer.
7. Flow in ~ 20 uL of polystyrene beads (at 20 pM, diluted in 4 mg / mL casein) coated with anti-digoxigenin and incubate for ~ 10 minutes.
8. Wash chamber with ~ 50 uL of sample buffer.
9. Flow in ~ 20 uL of polystyrene beads (at 20 pM, diluted in 4 mg / mL casein) coated with streptavidin and incubate for ~ 10 minutes.
10. Wash chamber with ~ 150 uL of sample buffer.

To ensure reasonable tethering efficiency, both anti-digoxigenin and streptavidin bead aliquots must be replaced with newly washed and diluted aliquots every 7-10 days to eliminate any free anti-dig or streptavidin that has desorbed from the surface of the bead.

Under the microscope, completed chambers contain a combination of single or double bead T-structure tethers. Longer trunks yield a larger percentage of double bead constructs due to a decreased probability of steric hindrance between the two beads during the stochastic double bead binding process. T-structure integrity may be tested by locating a double bead construct, trapping each bead in a separate trap and ensuring that the beads can be separated and are tethered to each other as well as to the surface of the cover slip.

Prior to unzipping of the template, both the fixed and steered PSDs are adjusted so that the undeflected beams are located at their centers. Next, the beads are loaded into the separate traps at low laser power to discourage beads sticking to the surface of the cover slip. Then the height of the trap center relative to the surface is fixed by manually adjusting the height of the microscope objective. The attachment point of the trunk may be centered via one of two ways: (1) the piezo stage may be manipulated along the X dimension and positioned such that the focus of the beads in each trap is identical; (2) the piezo stage can sweep through a range of positions along X and then repositioned at the location which corresponds to the point of symmetry in the corresponding force behavior of the two traps.

Unzipping was achieved by moving the steered trap at a constant velocity along the positive X direction. Meanwhile, the piezo was moved along the same direction at

half the velocity of the steered trap to ensure that the attachment point of the trunk did not lag behind. Data was collected at 200 Hz, which was a limitation imposed by the digital control of the XYZ piezo stage via the USB port in Windows 2000 as well as the calculation of X and Z forces in real-time as a potential feedback parameter.

***Data treatment: estimating the location of the DNA junction***

The dual beam trap has been fully calibrated in the XZ plane. Knowledge of the normalized X and Z signals in combination with the trap stiffness throughout the usable region of the XZ plane yields the X and Z displacements relative to the trap center and the X and Z forces applied to each bead. The force vectors on each bead are applied along the arms and, therefore, we can use this information to estimate the location of the DNA junction at each time point. Next, the extension of each arm is calculated from the displacement vector between the junction and the bead location after accounting for the radius of each bead. The force along each arm is used to estimate the total extension expected for dsDNA of known contour length for each arm using the Modified Marko-Siggia wormlike chain model[7] and that extension is subtracted from the total displacement. What remains is presumed to be the extension of ssDNA for each arm and should be equal for both arms. In the current T-structure design (Figure 4.2), the dsDNA contour length for each arm differs by almost 200 bp. Comparison of the ssDNA calculation for each arm permits the determination of which T-arm was in which trap by choosing the configuration which yields to closest match for both arms. Finally, the number of base pairs unzipped is taken as the average value calculated for both arms. Analogous to unzipping traces taken using the single beam optical trap, unzipping data taken in the dual beam trap appeared to be slightly shifted and elongated relative to their theoretical prediction and so traces were correlated by eye and a shift and stretch correction were added in each case. Figure

4.4b-d show representative traces obtained in this way. For each unzipping trace, several relevant forces are indicated, including the forces along the arms and their X and Z components, the force applied along the trunk and the force applied perpendicular to the trunk at the next unopened base pair. It should be noted that a proper theoretical treatment of the unzipping fork behavior is not yet currently available for unzipping segments experiencing a non-zero tension. That said, the general shape of the unzipping curve appeared to correlate well with the existing theoretical prediction with the exception that all calculated forces are noticeably higher than ~ 15 pN (Figure 4.4b-d).

***Data treatment: estimating trunk attachment point***

The attachment point of the trunk is calculated in the following way. First, the force applied to the trunk is computed via the superposition of the forces applied along each arm. The top of the trunk is taken as the estimated junction location, described previously. The current contour length of the trunk is calculated by taking the known contour length of the trunk (in base pairs) and subtracting the average number of base pairs calculated via the two arms, as above. The extension of the trunk is calculated by using the force along the trunk in conjunction with its current contour length (in base pairs). Lastly, the attachment point of the trunk to the cover slip is calculated by extending a vector from the estimation of the junction along the direction indicated by the force vector applied along the trunk. A good test of the accuracy of this technique is to compare the estimated location of the attachment point with the known behavior of the XYZ piezo stage. Figure 4.5 shows the results for two representative traces. Figure 4.6a shows a T-structure that has been unzipped while the XYZ stage was not moved. Notice that each estimate of the trunk attachment to the cover slip (Figure 4.5a, magenta) is located around the same position. Throughout the entire unzipping

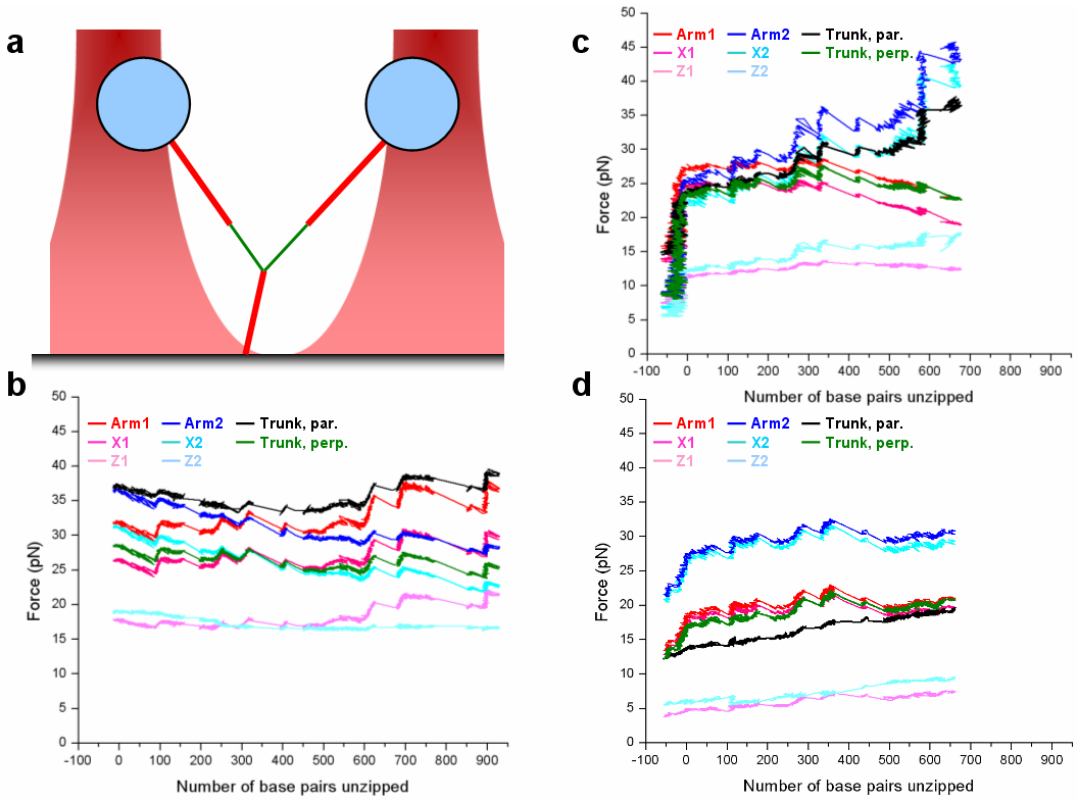


**Figure 4.4. Naked dsDNA unzipping via the T-structure.** (a) The geometry of the T-structure. The junction is estimated to be the apparent intersection point of the measured force vectors applied along the arms. The number of base pairs unzipped is computed by calculating the extension from the junction to the outer surface of the bead and subtracted the expected dsDNA extension. (b-d) Three representative T-structure unzipping datasets where various calculations of forces are indicated versus the calculated number of base pairs unzipped.

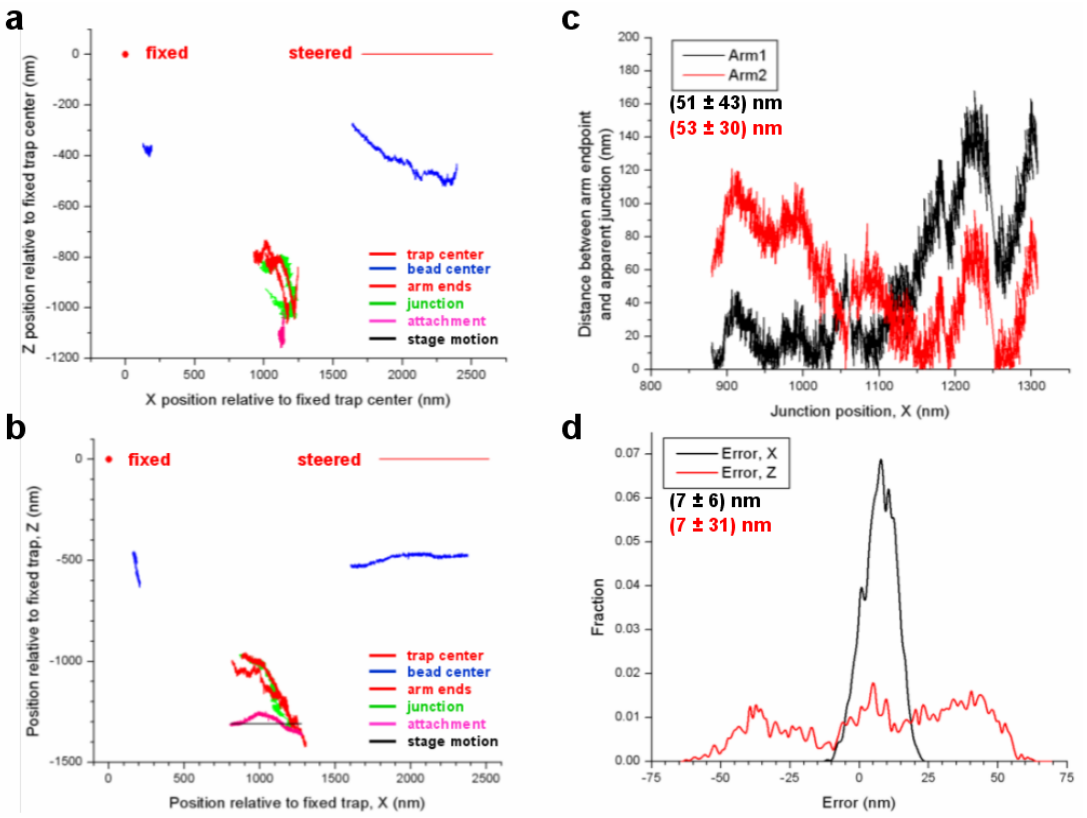


**Figure 4.5. Demonstrating the precision of calculating the apparent DNA junction and the trunk attachment point to the surface.** (a) The attachment point of the trunk to the surface is calculated to within 11 nm (STD) along X and 19 nm (STD) along Z in the case where the piezo stage remains still. (b) The attachment point is calculated to follow the behavior of a moving XYZ stage along X to within (7 ± 6) nm in X and (7 ± 31) nm in Z. (c) After calculating the number of base pairs in each arm, the end of each arm relative to the apparent DNA junction was calculated to within ~ 50 nm for both arms. (d) A histogram showing the displacement between the calculated attachment point of the trunk and the known XYZ piezo stage position.

segment, the mean calculated position is within 11 nm along the X dimension and within 19 nm along the Z dimension, which represents a measurement of the precision for the analysis.

Figure 4.5b shows a T-structure that has been unzipped while the XYZ stage was simultaneously moved along the positive X axis at a constant velocity. In this case, the estimated point of trunk attachment to the cover slip (Figure 4.5b, magenta) follows the known motion of the XYZ stage (Figure 4.5b, black) with noticeable systematic error in the Z dimension. To demonstrate the precision of this technique, a comparison of the calculated endpoint of each arm relative to the apparent DNA junction location was made and the calculated displacement was plotted versus the X position of the apparent junction location (Figure 4.5c). For both arms, the mean displacement was ~ 50 nm and this was typical for all data taken under constant X stage velocity. The error in the trunk attachment point was also calculated by comparing it to the known motion of the XYZ stage (Figure 4.5d). The attachment point relative to the XYZ stage position was calculated to be (7 ± 6) nm in the X axis and (7 ± 31) nm in the Z axis. This error was typical for all data taken under constant X stage velocity. Interestingly, there appeared to be systematic error in the calculation of the Z location of the trunk attachment point, but not in X.

***The T-structure as a means to generate single stranded DNA***

The T-structure provides a mechanism for the mechanical separation of dsDNA through the attachment of a single strand to the surface of a cover slip. This provides a very simple mechanism for the generation of long strands of ssDNA, which is otherwise very difficult to obtain. Figures 4.6a-d demonstrate how a long single stranded DNA can be produced by unzipping the T-structure to completion. In this

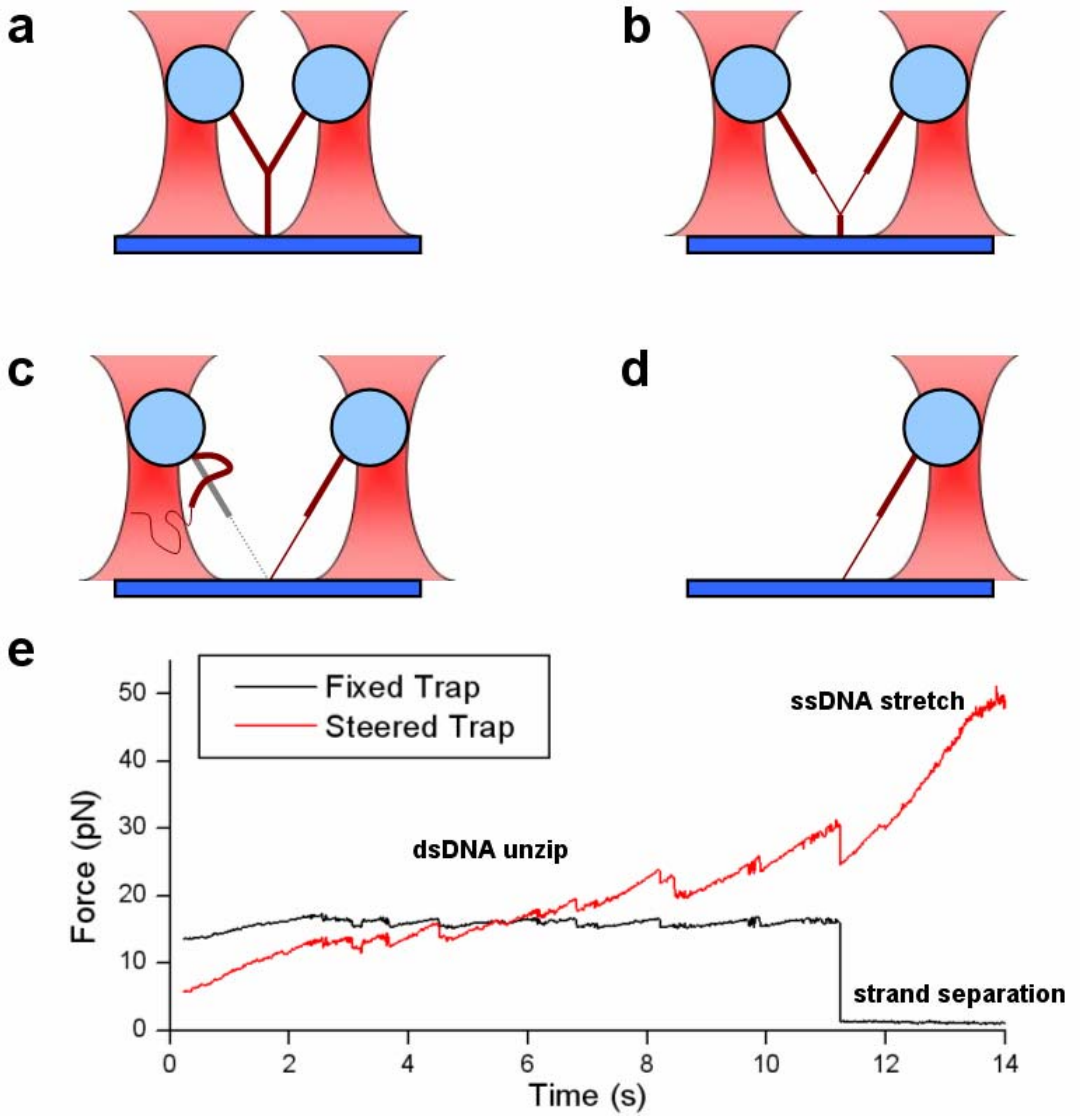


**Figure 4.6. The generation of long ssDNA segments by unzipping the T-structure to completion.** (a-d) An example of how a 950 bp ssDNA segment may be generated by unzipping the T-structure trunk to its completion. When the unzipping fork reaches the attachment point, one of the strands remain attached to the stage, permitting its further manipulation through either the steered trap (as shown) or the XYZ piezo stage. (e) Representative dataset demonstrating that the bead in the fixed trap came detached from the surface after completely unzipping the T-structure trunk, whereas the bead in the steered trap remained attached via the remaining ssDNA segment.

scenario, the opposite end of the fluorescein labeled strand happened to be trapped by the steered beam, allowing for further manipulation of the strand. However, the strand could also be manipulated via the fixed trap by manipulating the XYZ piezo stage in place of steering the beam. Figure 4.6e shows a representative example where dsDNA was unzipped to completion and then ssDNA was stretched in the steered trap until the bead fell out of the trap along the Z axis. Notice that the force measured by the fixed trap fell to zero after unzipping had completed, consistent with the bead in that trap being pulled into the trap center with no external forces other than Brownian motion. The bead in the other trap detected force behavior consistent with the extension of a flexible polymer.

***Future work***

The T-structure is a novel single molecule assay and its potential to expand the sphere of biological applications of optical tweezers is exciting. One study that would be immediately useful would be to explore the theoretical behavior of an unzipping fork while the unzipping segment is under an applied tension. This could offer a quantitative explanation as to why the unzipping forces observed in these experiments are significantly higher than the 15 pN typically observed when no tension is applied. Also, the generation of more accurate theoretical predictions would be useful during the alignment of data, as in the case for the single beam optical trap.

REFERENCES


1. La Porta A and Wang MD, Optical torque wrench: angular trapping, rotation, and torque detection of quartz microparticles. *Phys Rev Lett* **92**(19): 190801 (2003).
2. Forth S, Deufel C, Sheinin MY, Daniels B, Sethna JP and Wang MD, Abrupt buckling transition observed during the plectoneme formation of individual DNA molecules. *Phys Rev Lett* **100**(14): 148301 (2008).
3. Allemand JF, Bensimon D, Lavery R and Croquette V, Stretched and overwound DNA forms a Pauling-like structure with exposed bases. *Proc Natl Acad Sci U S A* **95**(24): 14152-7 (1998).
4. Sheinin MY et al., *Manuscript in preparation.*
5. Shundrovsky A, Single molecule studies of sequence-dependent transcription pausing. *Cornell University PhD Thesis* (2004).
6. Deufel, C. & Wang, M.D. Detection of forces and displacements along the axial direction in an optical trap. *Biophys J* **90**, 657-67 (2006).
7. Wang, M. D., H. Yin, R. Landick, J. Gelles and S. M. Block (1997). "Stretching DNA with optical tweezers." Biophys J **72**(3): 1335-46.

# Chapter 5
# A novel microfluidic chamber that produces a linear concentration profile

***Motivation for a flow cell that produces a chemical gradient***

Traditional optical trapping sample chambers are static. After assembling DNA tethers to the surface, the final experimental buffer is flowed in via pipette, by hand, and data is collected one single molecule at a time under identical conditions or until a different buffer is also flowed in via pipette, by hand. These chambers are very inexpensive and simple to produce. It allows a user to produce a sample chamber very quickly and to collect a lot of data without worrying about the additional complications introduced by having a microfluidic chamber.

On the other hand, a static sample chamber may present severe limitations under certain conditions. Some biological events occur very quickly after an exchange of buffer (RNA polymerase transcription after introduction of NTPs) and preparing a new chamber for the collection of one or two experimental datasets is extremely time-consuming. A lot of biological processes on both the molecular and cellular level depend upon the generation and existence of chemical gradients which cannot be maintained in a static chamber. Other processes depend upon the selective or reversible exposure to chemical or protein reagents, such as salt, NTPs, dNTPs, protein chaperones, RNA, etc.

Several approaches are common to achieve the selective exposure of samples to chemical reagents, especially rapid mixing devices and laminar flow cells. Rapid mixing approaches, stopped-flow instruments, are generally unsuitable for optical trapping and other single molecule techniques. Buffer exchange during an optical trapping experiment is possible manually by pipetting or through the construction of simple flow cell chambers, but often has the disadvantage of exposing the sample of interest to gradual changes of reagent concentration due to diffusion along the

direction of flow. The rate of exchange can be increased, but doing so exposes samples to higher forces due to viscous drag which have the potential to significantly perturb sensitive experiments. Laminar flow cells have been used in conjunction with optical trapping instruments for many years and they work well for achieving selective exposure of DNA to specific reagents[1,2,3,4]. However, they also suffer from the drawback of continuously exposing samples to small constant forces. Furthermore, although laminar flow cells have been used to generate chemical gradients in a variety of ways, the quantitative description of these gradient fields are relatively complicated as a result of diffusion both along and perpendicular to the flow.

We have developed a flow cell capable of generating a well-defined linear concentration profile via chemical diffusion across a channel that does not experience any net flow. This channel is compatible with our stretching and unzipping optical trapping experiments and has been shown to be stable for at least 48 hours of flow. Furthermore, the microfabricated dimensions of the channels ensure that very little sample product is required, saving precious reagents such as purified protein.

***Operating principle: generation of a linear gradient***

Two parallel channels are connected via a perpendicular channel and the pressures at the inputs of each channel are adjusted such that the pressures at either side of the connecting channel are equal. Under that condition, there is no fluid flow across the channel. If a reagent (e.g. salts, proteins, etc.) is introduced into one of the input channels, some of it passes through the connecting channel via diffusive flux (as opposed to convective flux) (Figure 5.1a). The steady state solution for the concentration profile will be linear, shown as follows. The diffusion equation in one dimension is:

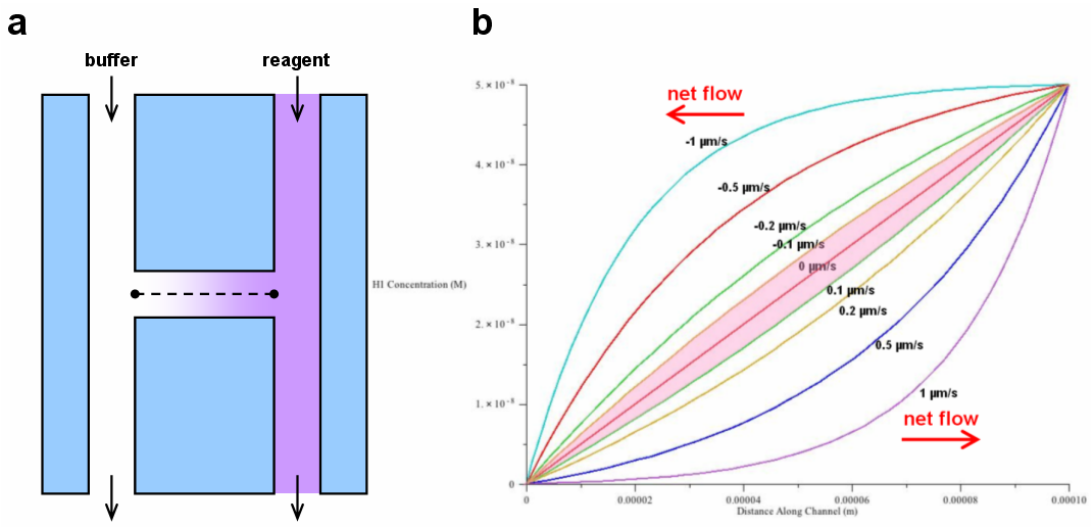


**Figure 5.1. The operating principle underlying a flow cell that produces a linear concentration profile along a channel exhibiting zero net flow.** (a) If two parallel channels are connected via a perpendicular third channel, zero net flow will exist in the connecting channel if the pressures on either side are equal. If a chemical reagent is added to one of the parallel channels, there will be diffusive flux through the connecting channel (but no convective flux) and the concentration profile will be linear at steady state. (b) Solving the diffusion equation along the connecting channel for variety of net flow rates. The concentration profile is plotted for a 100 um long channel, as indicated by the dotted line in (a) and the profile is perfectly linear when the net fluid flow is zero.

$$\frac{\partial \varphi(x,t)}{\partial t} = D\frac{\partial^2 \varphi(x,t)}{\partial x^2} - v\frac{\partial \varphi}{\partial x} \tag{5.1}$$

At steady state, the time derivative is zero and integration yields

$$\frac{D}{v}\ln[\varphi(x) + C_1] = x + C_2 \tag{5.2}$$

Using the boundary conditions,

1. $\varphi(x = 0) = 0$ (5.3)
2. $\varphi(x = L) = C_0$ (5.4)

allows us to solve for the concentration at steady-state when a constant flow rate, $v$, is present along $\hat{\mathbf{x}}$:

$$\varphi(x) = \frac{C_0}{1 - \exp\left(\frac{vL}{D}\right)}\left[1 - \exp\left(\frac{vx}{D}\right)\right] \tag{5.5}$$

This equation for various choices of net flow velocity with a source concentration of H1 linker protein of 50 nM with known diffusion coefficient (D = 20 $\mu m^2\ s^{-1}$).

***Channel layout for optical trapping purposes***

For practical use as part of an optical trapping setup, the channel layout is a little more complicated, as shown in Figure 5.2. The final design consists of four input channels, one each for alpha-digoxigenin coated beads that have been preassembled with single strands of DNA, plain sample buffer, a reagent or protein of interest and streptavidin coated beads. Dual bead DNA constructs would first be assembled in the plain buffer channel and then introduced into the connecting channel and exposed to a particular concentration of the desired reagent. This device is designed to operate with only two pressure sources: one source hooked up to both the buffer and reagent inputs and the other hooked up to the alpha-dig and streptavidin coated bead inputs. A microfluidics simulation performed in COMSOL shows that the two pressure sources may be

adjusted to control the rate of flow of protein and beads separately without affecting the concentration profile in the connection channel (except for cases when the pressure source affecting the bead channels is significantly higher) and this has been confirmed via direct observation. COMSOL also confirms the results of the theoretical prediction – that the velocity across the connecting channel is zero (Figure 5.2a) while the concentration profile achieves a linear steady state solution (Figure 5.2b).

***Microfabrication protocol***

Because of the precise pressure control required at either end of the connecting channel, we decided to microfabricate the devices so that the paths on either side of the connecting channel were as identical as possible. This permitted the use of a single pressure source for the two parallel channels, which has the advantage that any fluctuations in pressure at the source are transmitted to both sides of the channel simultaneously and no active control is required. To be compatible with our optical trapping apparatus, both the top and bottom surfaces of the flow cell need to be optically transparent, so fused silica was chosen as the substrate. Dry etching was chosen over wet etching to avoid the curved surfaces that result from isotropic etching that would refract the beam. Channel widths were chosen to ensure that the beam does not experience deflection due to refraction at the sidewalls during the manipulation of a fully extended dsDNA or ssDNA molecule. Channels were etched to at least 12 um deep to reduce the probability of beads sticking to either surface during exposure to high laser powers during optical trapping experiments. An outline of the final protocol is provided below. A simplified outline is shown in Figures 5.3a-f with SEM images of some of the final devices in Figures 5.3g-j.

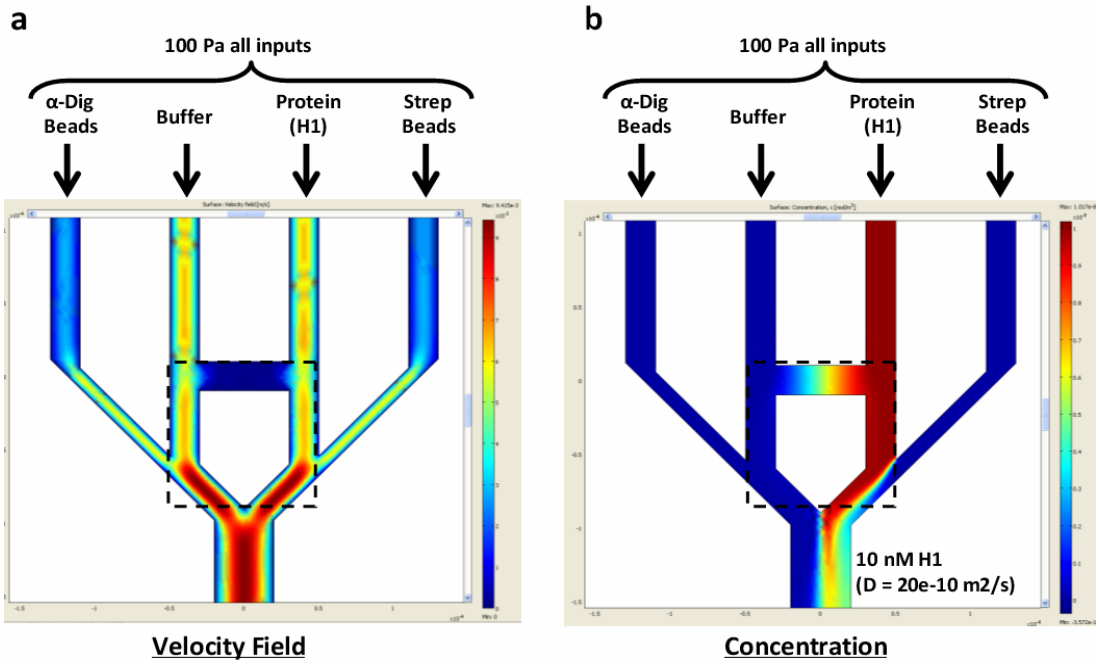


**Figure 5.2. COMSOL simulations of a flow cell that produces a linear concentration profile.** (a) The velocity field for the final flow cell design and an equal pressure applied across all four inputs. Notice the lack of flow predicted across the connecting channel, as expected. (b) The concentration profile across the channel is predicted to be linear, as expected. The profile does not change appreciably unless the ratio of pressures applied to the outer channels compared to the inner channels is much greater than unity. The area indicated by the dotted lines shows the maximum range of the XYZ piezo stage in the XY plane.

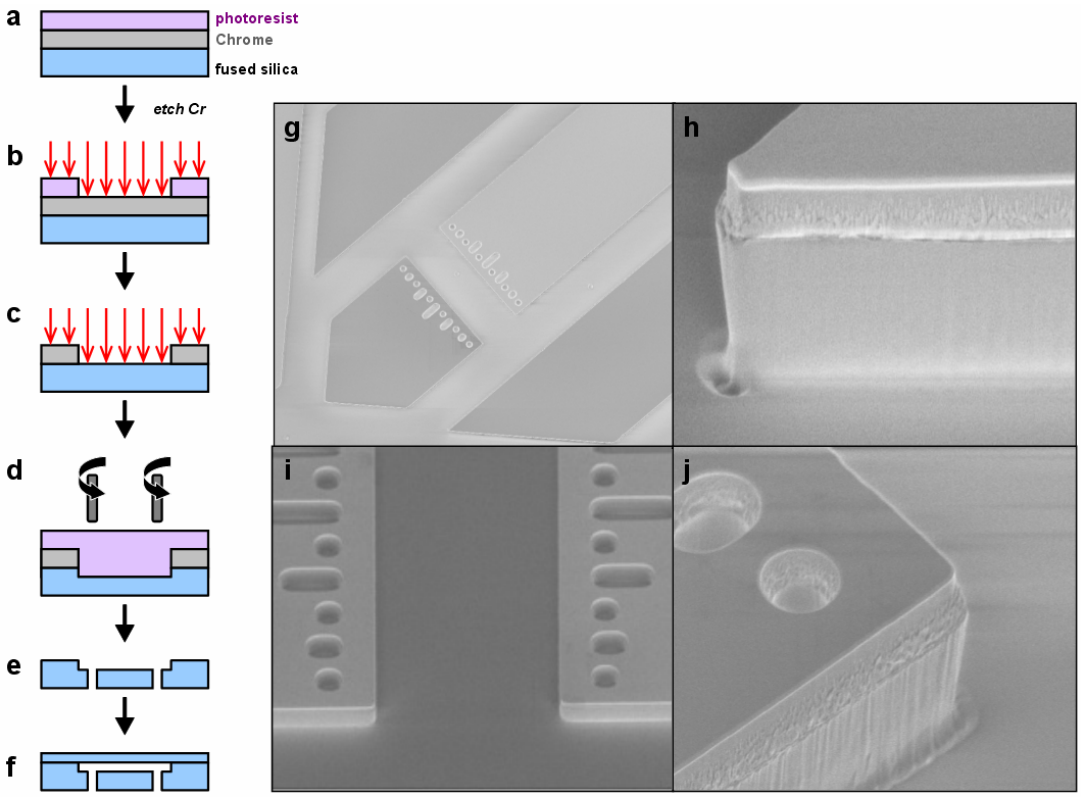


**Figure 5.3. Fabrication of flow cells capable of generating a linear concentration profile with zero net flow.** (a) Layers of Cr and photoresist are deposited onto fused silica wafers. (b) PR is developed and used as a mask until the Cr layer is etched down to the fused silica. (c) Remaining PR is stripped and fused silica is plasma etched. (d) PR is coated over the surface to protect the channels while holes are drilled through the wafer via diamond-tipped bits. (e) PR and Cr are removed. (f) A 170 um thick fused silica wafer is bonded over the etched channels and the resulting devices are annealed at 1100C. (g-h) SEM images of the completed devices just prior to wafer bonding.

1. Clean 100 mm diameter, 1 mm thick fused silica wafers (Mark Optics, Santa Ana, CA) via RCA treatment.
2. Deposit an etch mask by sputtering ~ 375 nm of Cr.
3. Spin on SPR-220-3.0 photoresist @ 2000 RPM, 1000 RPM/s, for 60 s. Soft bake at 115°C for 90 s.
4. Expose through photomask on contact aligner for 6.5 s.
5. Post exposure bake at 115°C for 90 s.
6. Develop resist using 300 MIF for 120 s. Check under microscope and repeat, if necessary.
7. Etch through the Cr layer using the resist as an etch mask.
8. Strip remaining photoresist layer by in the Hot Bath for ~ 20 mins. Rinse and dry.
9. Standard Hot Piranha clean to remove any residue from the Hot Bath.
10. Etch channels in fused silica wafer with Cr mask using AR/CHF3 plasma.
11. Spin on a protective layer of SPR-220-3.0 at 2000 RPM, 1000 RPM/s, for 60 s. Soft bake at 115°C for 90 s.
12. Use a diamond-tipped bit (Starlite Industries, McMaster-Carr #4376A11) at high RPM (> 9000) to manually drill holes through the wafer by hand. Use an aluminum jig to ensure that the holes are aligned with locations on the wafer.
13. Remove machining oil and debris by sonication in 95% ethanol for 30 mins.
14. Clean wafers in Hot Bath for 20 mins followed by standard Hot Piranha treatment.
15. Strip remainder of the Cr mask layer using “Cr Etchant” for 2+ hours.
16. Bond the 1 mm thick etched fused silica wafers to clean, 100 mm diameter, 170 um thick, fused silica wafers (Mark Optics, Santa Ana, CA).

17. Anneal bonded wafers for 2 hours in $N_2$ gas at 1100°C in a MOS clean furnace.
18. If individual flow cells are desired, a dicing saw may be used. Be sure that an all-purpose blade is installed with a cutting depth of at least 1170 um.

***Attaching microfabricated flow cells to external pressure***

External pressure sources were attached to microfluidic devices by inserting metal tubing into pre-punched holes in PDMS (Figure 5.4). PDMS was degassed and cured at 60C for 90 minutes on a silicon wafer patterned with 50 um high SU-8 pillars that matched the layout of hole positions on the bonded fused silica wafers. After cooling, the PDMS was cut with a scalpel into two pieces, as shown in Figure 5.4, and holes were punched through the indentations left by the SU-8 mold. Both pieces of PDMS were plasma cleaned along with the side of the wafer to be bonded. The pieces of PDMS were aligned one at a time via an XYZ micrometer stage to the wafer and pressed with ~ 10 lbs of force for several minutes. The completed product (Figure 5.4) provides an array of devices with rows of holes to be used to connect to specific devices of choice. The large gaps in PDMS are required to accommodate the rather large Nikon oil immersion condenser lens which will provide optical contact at the top of the wafer during an experiment.

***Demonstration of gradient generation***

As a demonstration that the completed devices work as designed, 489 nm diameter polystyrene beads were introduced into all four input channels to visualize the flow and fluorescein was diluted and introduced as a reagent into the protein channel. The same constant pressure source was connected at all four input channels. Typically it takes several minutes to evacuate the existing air from all the channels before a steady flow is achieved.

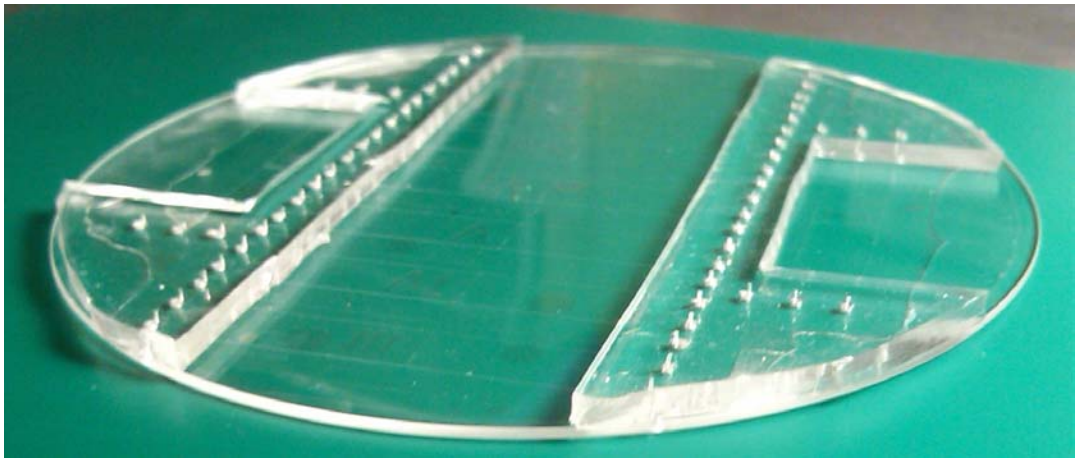

**Figure 5.4. PDMS bonded to completed devices on a wafer.** PDMS was degassed, cured at 60C for 90 minutes and then allowed to cool at room temperature for several minutes before being plasma cleaned with the fused silica wafer, aligned and pressed together with ~ 10 lbs of force for at least 10 minutes. Finally, the bonded PDMS-fused silica product was annealed at 60C for ~ 2 hours making the bond permanent. The wafer was mounted as is onto a microscope stage and an oil immersion condenser lens was brought into contact with the fused silica wafer at the gaps between pieces of PDMS. Sample volumes are loaded into PEEK tubing and connected to holes in the PDMS via steel tubing that has been bent 90 degrees. Mating of steel tubing to PDMS holes is tight enough to withstand positive pressure exceeding 40 psi.

Figure 5.5 demonstrates a typical concentration profile for these devices. Figure 5.5a demonstrates that the fluid flow lines do not enter the connecting channel. The white dots are images of beads that were accumulated via image acquisition over ~ 30 seconds at 30 seconds. Thus, the fluid flow across the channel is nearly zero. The single bead that existed in the channel over the course of the image acquisition shown here experienced motion consistent with random walk diffusion associated with Brownian motion.

Upon uniform excitation of the device, fluorescein emission was measured and the results are displayed in Figures 5.5b-d for three different orientations for clarity. The channel containing the fluorescein source displayed the highest intensity, whereas the channel containing only buffer displayed almost zero intensity, as expected. The connecting channel, as predicted by theory, exhibited a linear concentration profile. For the particular device demonstrated in Figure 5.5, the gradient remained stable after more than 48 hours of continuous flow. The performance from device to device can vary somewhat. Most devices operate as designed and demonstrated here with a single pressure source for both the buffer and reagent channels, but some devices required the use of additional pressure sources to allow independent control over the buffer and reagent channels to introduce a slight pressure offset and achieve a zero net flow condition. I attribute these subtle variations to differences in the way the tubing and PDMS connections are mounted at the holes providing external access to the microchannels.

***Future work***

I have designed and constructed a microfabricated flow cell compatible with our existing optical trapping setups and have demonstrated that it is capable of generating

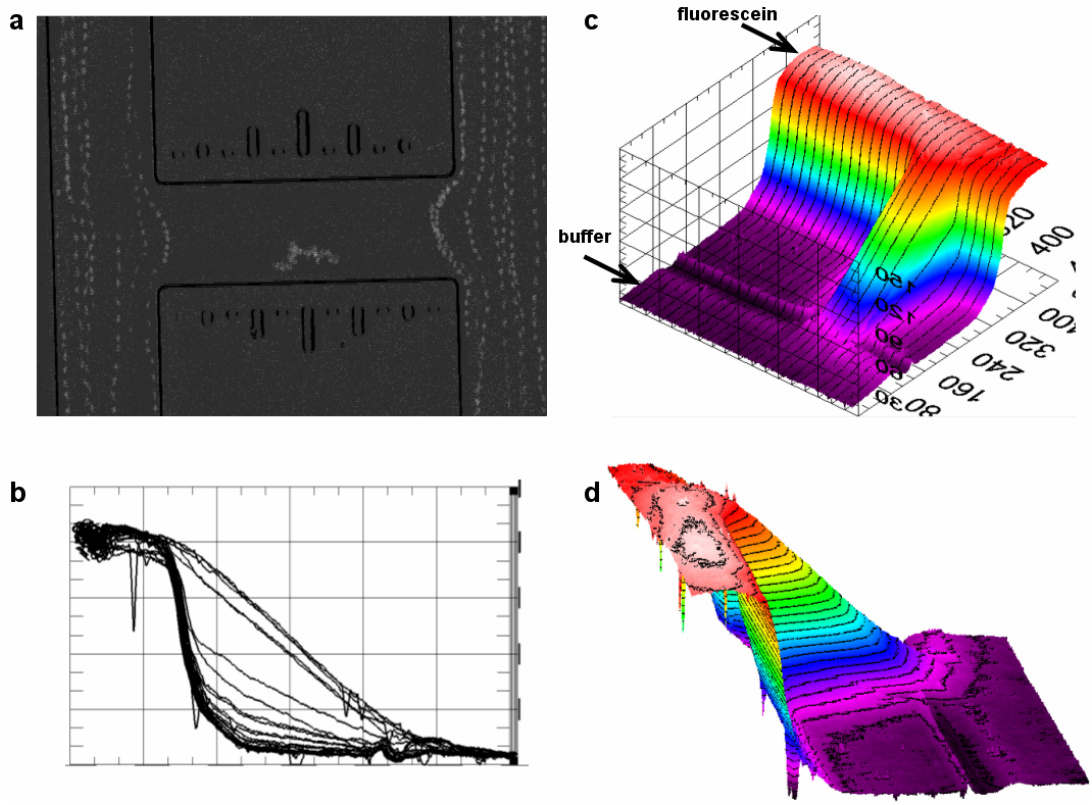


**Figure 5.5. Demonstration of a linear gradient.** Fluorescein was introduced into one of two parallel channels and 489 nm polystyrene beads were introduced into both parallel channels. (a) Time lapse photos were taken and summed together at 30 Hz to plot out the fluid flow lines, demonstrating zero net flow in the connecting channel. Notice a single bead in the connecting channel undergoing random motion consistent with Brownian fluctuations. (b-d) When the device was uniformly excited by UV light, fluorescence intensity was detected. As expected, the intensity was greatest for the channel containing fluorescein, lowest in the channel containing sample buffer and a linear gradient was observed in the connecting channel.

a linear chemical concentration profile along a channel that does not experience any net fluid flow. The next immediate step is to develop an appropriate DNA tethering protocol around the existing design which ensures a high efficiency of single DNA tether formation between alpha-digoxigenin and streptavidin coated beads.

REFERENCES


1. Wuite GJ, Davenport RJ, Rappaport A and Bustamante C, An integrated trap/flow control video microscope for the study of single biomolecules. *Biophys J* **79**(2):1155-67 (2000).
2. Bianco PR, Brewer LR, Corzett M, Balhorn R, Yeh Y, Kowalczykowski SC and Baskin RJ. Processive translocation and DNA unwinding by individual RecBCD enzyme molecules. *Nature* **409**(6818):374-8 (2001).
3. Brewer LR and Bianco PR, Laminar flow cells for single-molecule studies of DNA-protein interactions. *Nat Methods* **5**(6): 517-525 (2008).
4. Amitani I, Liu B, Dombrowski CC, Baskin RJ, and Kowalczykowski SC, Watching individual proteins acting on single molecules of DNA. *Methods Enzymol* **472**:261-291.